
Imaging Infrared Detectors II

20001218 083


MITRE

Imaging Infrared Detectors II

Study Leader:
R. Westervelt

Contributors Include:
H. Abarbanel
R. Garwin
R. Jeanloz
J. Kimble
J. Sullivan
E. Williams

October 2000

JSR-97-600

Approved for public release; distribution unlimited.

JASON
The MITRE Corporation
1820 Dolley Madison Boulevard
McLean, Virginia 22102-3481
(703) 883-6997

Contents

| | |
|---|-----------|
| 1 INTRODUCTION | 1 |
| 2 IMAGE CHARACTERIZATION | 5 |
| 3 UNCOOLED MICROBOLOMETER ARRAYS | 11 |
| 4 QUANTUM WELL INFRARED PHOTODETECTORS | 17 |
| 5 HgCdTe PHOTODETECTOR ARRAYS | 21 |
| 6 DEVELOPMENTS | 23 |
| A FUNDAMENTALS OF INFRARED DETECTOR PERFOR- MANCE | 27 |
| A.1 Blackbody Radiation | 27 |
| A.2 Temperature of Operation | 33 |
| B APPENDIX: IMAGING BOLOMETER ARRAYS | 43 |
| B.1 Bolometer Noise | 44 |
| B.2 Comparison of Bolometers with Quantum Detectors | 47 |
| B.3 Responsitivity | 49 |
| C APPENDIX: THERMOELECTRIC MATERIALS | 53 |
| D APPENDIX: WORKSHOP PARTICIPANTS | 65 |

1 INTRODUCTION

JASON has been tasked by the Army to review recent progress in infrared detector technology and to update the earlier JASON report "Imaging Infrared Detectors" (JSR-91-600). To this end, a workshop was conducted during the 1997 Summer Study with distinguished participants drawn from industry, academia, and government, listed in Appendix D. Through discussions with workshop participants and the JASONs an updated overview of the state of imaging infrared detector technology was developed, and is presented in the body of this report as follows: Section 2 (Image Characterization); Section 3 (Uncooled Microbolometer Arrays); Section 4 (Quantum Well Infrared Photodetectors); Section 5 (HgCdTe Photodetector Arrays); and Section 6 (New Developments). Appendices to the original report contained primers on infrared basics, which have been proven to be useful. The current report contains updated versions: Appendix A (Fundamentals of IR Detector Performance); Appendix B (Imaging Bolometer Arrays); and a new addition, Appendix C (Thermoelectric Materials).

Imaging infrared detector technology has advanced rapidly. Important developments:

- Driven by the need for image recognition, large staring long wave infrared (LWIR) arrays have been developed: 320×240 pixel uncooled bolometer, and cooled quantum well infrared photodetector (QWIP), and cooled HgCdTe detector arrays are available as deliverable products; 640×480 pixel arrays have been demonstrated for the QWIP and HgCdTe technologies. Larger arrays up to high density television (HDTV) are planned for all three approaches.

- Uncooled bolometer and cooled QWIP cameras with excellent performance are commercially available, both inside the U.S. and abroad.
- Two “color” (e.g. LWIR and MWIR) detector arrays are under development, with two color pixel demonstrations for the QWIP and HgCdTe technologies.
- Continued improvements in Si readout integrated circuits (ROIC) have led to better uniformity and sensitivity.
- Methods for mechanical strain relief between the detector array and the Si ROIC have been developed – e.g. using thinned detector materials and ROIC strain matching – for improved reliability.

Recent advances in infrared camera technology will have substantial impact on the Army:

- Uncooled IR cameras now offer performance traditionally associated with cooled HgCdTe units, but at relatively low prices. They are light weight, have low power consumption, and produce excellent images with good sensitivity (noise effective temperature difference NETD ~ 70 mK with f/1 optics). In the military uncooled IR cameras will be the natural choice for small unit operations, surveillance, and even some targeting applications. These cameras have many possible commercial applications – such as security, fog penetration, and night driving – which may drive future development work. The international availability of uncooled technology will soon change “owning the night” to “sharing the night.”
- QWIP technology has been used to make small, portable LWIR cameras using miniaturized coolers. Advantages of QWIP arrays are excellent image quality due to high uniformity, and a mature material technology permitting the production of large arrays (640×480 pixels)

and complex pixel structures for multi-color and polarization sensitive detectors. However, their quantum efficiency is limited to relatively small values by fundamental considerations, requiring cooling to 70 K and below for best sensitivity.

- Large staring HgCdTe LWIR cameras with 640×480 pixels have been demonstrated. These instruments have excellent image quality and high sensitivity, and would be the natural choice for sensitive IR telescopes to be used for surveillance and targeting at long ranges. These arrays are impressive demonstrations of progress in HgCdTe technology. But they are expensive, and their use will be limited to the most demanding applications while relatively inexpensive uncooled cameras will suffice for most applications. The fabrication technology for LWIR HgCdTe detectors is still not fully mature, and difficulties remain.

2 IMAGE CHARACTERIZATION

The requirements placed on infrared cameras by Army applications can be quite different than airborne or strategic applications. The central function of infrared cameras for Army use is the detection and recognition of desired images – soldiers, fixed and mobile military equipment – in the presence of spatial clutter – grass, trees, rocks, civilian cars and trucks. Camera noise and nonuniformity also produce a type of clutter. The detection of small, featureless targets, such as missile exhausts, is also important, but does not play the dominant role it does in space. For the separation of images from clutter, the spatial characteristics of the image and the detector array are as important as the temporal characteristics.

The push toward larger detector arrays with more pixels in recent years has been driven by the realization that many pixels on target are needed to separate important images from clutter. A single bright pixel is probably not meaningful in the presence of clutter, unless it has additional spatial characteristics (e.g. rapid motion) to identify it. An image of a military target, such as a tank, with enough pixels for recognition, can be separated from the background without additional information. Even more pixels are desirable to identify the target, distinguish friend from foe.

For terrestrial use, balanced figures of merit which give equal weight to spatial and temporal “noise,” are needed to evaluate infrared imager performance. Traditionally, infrared detectors have been evaluated primarily by their temporal noise through figures of merit like the noise effective power (NEP) and the NETD of a single pixel. Spatial “noise” such as non-uniformity and fixed pattern noise has not been given equal emphasis, even though spatial “noise” can dominate the subjective image quality. Better, balanced figures of merit are needed to evaluate and compare the performance of infrared imagers. A possible example is the spatio-temporal power

spectrum $S(\vec{k}, \omega)$ where \vec{k} is the two-dimensional spatial wavevector across the image plane, and ω is the temporal frequency. The dependence of the power spectrum $S(\vec{k}, \omega)$ on the magnitude of \vec{k} could distinguish white, power law ($1/f^\alpha$), and periodic spatial noise, and plots of constant $S(\vec{k}, \omega)$ surfaces in the three dimensional \vec{k}, ω space would uncover and characterize spatial anisotropy, and spatio-temporal characteristics like diffusion and cross-talk. The use of spatio-temporal power spectra for characterization is standard in physics and materials science for systems with linear responses. For detectors (and for the field of computer vision) in which non-linear effects can be important, other approaches may be better, and should be explored. But over-simple characterizations of the spatial characteristics of infrared detector arrays (e.g. the “nonuniformity” is X%) are unlikely to be adequate.

Recognition of targets and threats is the most important function of infrared cameras for military users. The recognition range is related to detector sensitivity (NEP) in a simple manner explained below, but this connection is not easily summarized in a single graph. To understand the relationship, consider the problem of target identification and recognition for a tank moving toward the user from far away, first without atmospheric attenuation due to water vapor, fog and other obscurants, and then with attenuation. Figure 1 illustrates the situation for parameters appropriate to an uncooled LWIR camera. At long ranges R , the tank fills less than one pixel of the detector array, the temperature sensitivity increases as the tank moves closer as $\text{NETD} \propto 1/R^2$, and the target recognition range R_R increases with detector sensitivity as $R_R \propto 1/\sqrt{\text{NEP}}$. In this long range limit, the detection range for point-like objects increases with sensitivity, according to the conventional picture. However, once the tank occupies more than one pixel of the image, the temperature sensitivity NETD becomes *independent* of range R , as indicated in Figure 1. The reason is that the $1/R^2$ increase in photon flux from the tank at short ranges R is cancelled by the increase in number of pixels occupied by the image. If one can see the tank 100 ft. away in clear weather,

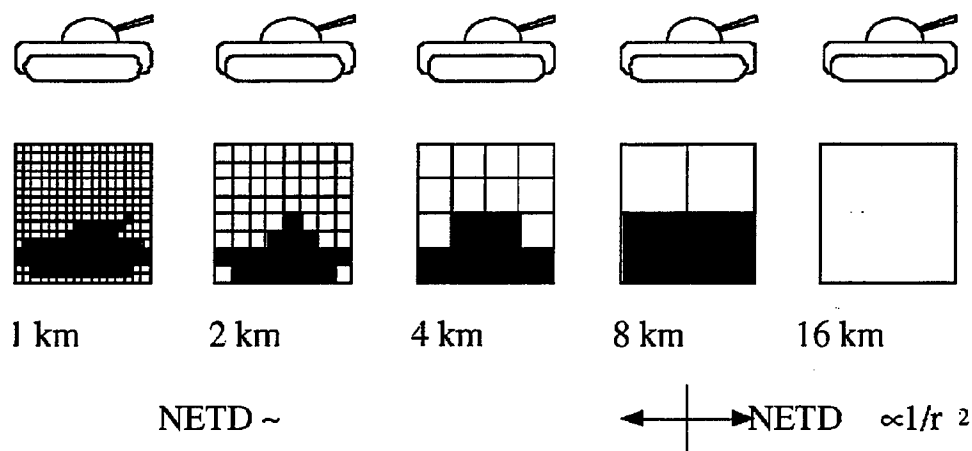


Figure 1: Illustration of the importance of pixels on target for image recognition, and of the behavior of noise effective temperature difference (NETD) with range. This example assumes typical uncooled camera specifications: 100 mm focal length, $\sim 10^\circ$ field of view, and $50 \mu\text{m}$ pixels, which give ~ 1 m spatial resolution at 2 km.

one can also see and identify it at 1 km, 2 km, and longer ranges, until it disappears into a point in one pixel, as illustrated in Figure 1, in accord with everyday experience. It is this many-pixels-on-target regime that is most important for Army applications. In this regime the recognition range is *independent* of detector sensitivity (NEP) for signal to noise ratios $S/N \gg 1$ in each pixel; if a target can be seen at short range, it can be seen at all ranges until it disappears into a point. Detector sensitivity becomes important in setting the intensity threshold for recognition at any range. Less infrared flux is received from the target for small pixel sizes, such as the $25 \times 25 \mu\text{m}^2$ pixels now entering production to increase array size within chip area limits, and for smaller numerical aperture optics, required by size and weight considerations for infrared telescopes. Thus the effect of detector noise for clear atmospheric conditions is to place lower bounds on pixel size and numerical aperture, not to limit recognition range.

Often targets are obscured by absorption and scattering due to water vapor, fog, smoke, and other aerosols, particularly under battle conditions. Under these circumstances the transmitted infrared photon flux falls more rapidly, and can be often characterized by an exponential attenuation length R_A . The attenuation length varies greatly with atmospheric conditions. To illustrate the effects on recognition, again consider a tank approaching from far away, but under foggy conditions. Initially its image size in the camera is less than one pixel, and the temperature sensitivity falls off with range as $\text{NEPD} \propto \exp(-R/R_A)/R^2$. When the image size reaches one pixel (at range R_1 determined by camera optics), the tank may or may not be detectable, depending whether $R_1 \leq R_A$ for which it can be detected (see above), or whether $R_1 \gg R_A$ for which it cannot. If the detector does not have sufficient sensitivity to detect the tank at range R_1 , then it remains undetected at shorter ranges, until it emerges from the fog all at once at a relatively large image size, again in accord with common experience. When target recognition is dominated by atmospheric attenuation rather than pixels on target, the recognition range increases with detector sensitivity as $R_R = R_A \ln(C/\text{NEP})$, where C is a constant determined by the target emission strength and camera optics. This expression can be more complex if forward scattering is important. The recognition range R_R is determined primarily by atmospheric absorption through R_A , and secondarily by detector sensitivity through the logarithmic dependence on NEP.

Connections between target recognition range and detector sensitivity have important implications for the choice of detector technology. High sensitivity is desirable for long recognition ranges under poor atmospheric conditions, and for cameras with small numerical apertures: it appears that HgCdTe will remain the technology of choice for infrared telescopes, long range sights, and other demanding applications. Uncooled arrays have become competitive with HgCdTe when recognition at very long ranges is not required, and uncooled technology may well come to dominate the majority

of infrared camera applications. When the sensitivity of uncooled arrays is adequate to produce a good image with available optics, the lower NEP of HgCdTe detectors has little advantage in recognition range: R_R is nearly independent of NEP in a clear atmosphere, and increases only logarithmically with NEP with atmospheric attenuation. High spatial uniformity and the lack of defects can be more important to target recognition than NEP under these conditions. It is here that QWIP detectors have an advantage, despite their low quantum efficiency. QWIP technology is particularly well suited to complex pixel designs for multi-color and polarization sensing arrays.

3 UNCOOLED MICROBOLOMETER ARRAYS

The development of uncooled microbolometer arrays started as a secret program, which was later declassified and transferred to commercial production. The idea is simple: to use modern lithography and processing techniques to fabricate large arrays of small temperature sensing bolometers. Two approaches were originally developed: bolometer arrays with resistive response (Honeywell) and arrays with ferroelectric response (Texas Instruments). Figure 2 is a drawing of one pixel of the original Honeywell concept – pixels of similar geometry are now made in a monolithic process by Texas Instruments using ferroelectric sensors. As shown, the temperature sensing element is thermally isolated above the readout circuitry by using long thin legs, which also provide electrical connections. This arrangement provides a high fill factor. The entire array is made in a monolithic process, based on standard Si processing with the addition of materials needed for resistive or ferroelectric sensing of the temperature.

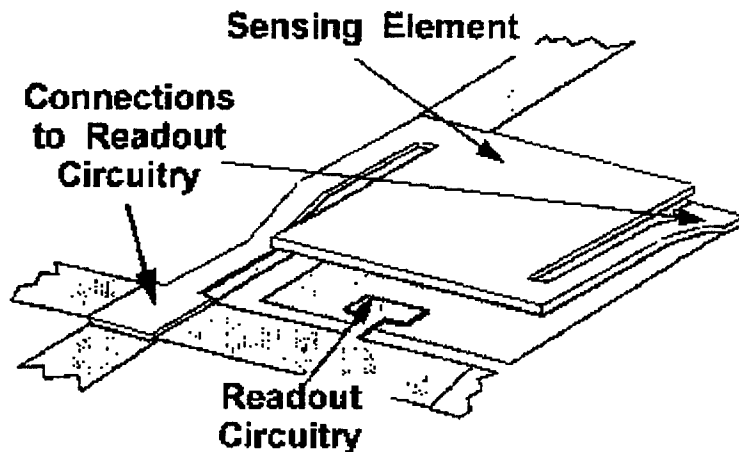


Figure 2: Diagram of a bolometer pixel from an uncooled bolometer array.

Of all the types of infrared detectors, uncooled microbolometer arrays are likely to have the largest impact on Army operations. That is because microbolometer arrays combine very good quality imagery with the low cost and ease of use associated with uncooled detectors. Although their sensitivity does not approach that of the best HgCdTe detector arrays, uncooled bolometer arrays provide a level of performance that is adequate for perhaps a majority of applications. Because microbolometer arrays are available internationally on a commercial basis, one can no longer assume that an adversary lacks good night vision capability.

Although uncooled bolometers are commonly considered to be insensitive compared with cooled quantum detectors such as HgCdTe, they can provide surprisingly good performance. As detailed in Appendix B.1, the square of the infrared noise equivalent power (NEP) for a bolometer is $\langle \delta P_{th}^2 \rangle = 4k_B T^2 G \Delta f$, where k_B is Boltzmann's constant, G is the thermal conductance between the bolometer element and the substrate, and Δf is the bandwidth. For quantum detectors the square of the NEP is $\langle \delta P_\gamma^2 \rangle = 2P_\gamma h\nu \Delta f$ with P_γ the absorbed infrared power, and $h\nu$ the photon energy. The ratio is

$$\frac{\langle \delta P_\gamma^2 \rangle}{\langle \delta P_{th}^2 \rangle} = \frac{1}{2} \left(\frac{\Delta T_\gamma}{T} \right) \left(\frac{h\nu}{k_B T} \right) \quad (3-1)$$

where ΔT_γ is the temperature increase in the bolometer produced by illumination. Comparing the two types of detector, we find that the square of the NEP is larger for quantum detectors by the ratio of the photon energy to the thermal energy, $h\nu/k_B T \sim 4$ for LWIR detectors, but smaller by the factor $\Delta T_\gamma/T$. Better bolometer performance is obtained with larger ΔT_γ , which can be increased with faster optics and lower thermal conductance. For current microbolometer arrays $\Delta T_\gamma \sim 1$ K, giving $\delta P_\gamma/\delta P_{th} \sim 0.1$ and an ideal limiting performance NETD ~ 10 mK for uncooled bolometers vs. NETD ~ 1 mK for quantum detectors. The actual performance achieved is somewhat less than NETD ~ 75 mK, due to excess noise in the bolometer element and readout circuitry.

Areas for improvement in microbolometer performance are higher bolometer responsivity (for lower noise), better thermal isolation (for higher induced temperature rise), and smaller heat capacity (for faster response).

High responsivity materials are needed for bolometers to provide a large signal and large signal-to-noise ratio. For resistive bolometers the responsivity is characterized by the dimensionless quantity $\alpha = (T/R)dR/dT$. The ratio of intrinsic thermal fluctuation noise to Johnson noise in the temperature sensor is

$$\frac{I_B^2 \langle \delta R^2 \rangle}{\langle \delta V_J^2 \rangle} = \alpha^2 \left(\frac{\Delta T_B}{T} \right) \quad (3-2)$$

where I_B is the bias current, δR is the resistance change due to thermal fluctuations, δV_J is the Johnson noise voltage, and ΔT_B is the temperature rise produced by the bias current. From this expression we see that high responsivity and large bias currents are desirable to overcome the intrinsic Johnson noise of resistive sensor elements. Comparing different classes of resistive materials (see Appendix B.1) we find $\alpha \sim 1$ for metals, $\alpha \sim -E_{act}/k_B T$ for semiconductors with E_{act} the activation energy, and $\alpha \sim -(1/4)(T_0/T)^{1/4}$ for variable range hopping materials like VO_x . The parameter T_0 characterizes variable hopping in the material used. Cooled semiconductors provide excellent responsivity, but the best response for uncooled resistive detectors is obtained with materials like VO_x for which $\alpha \sim 6$. Using this value of responsivity we find that significant heating by the bias current $\Delta T_B \sim 8K$ is needed to avoid domination by Johnson noise. To avoid excessive power consumption by the array, the bias current can be pulsed during readout.

Materials that exhibit a phase transformation near the temperature of operation are natural candidates to provide higher thermal responsivity. The approach used by Texas Instruments relies on a ferroelectric phase transition near room temperature to obtain high responsivity. Phase transitions in resistive sensors are good candidates to improve performance. The superconducting transition in high T_c materials results in a strong thermal

response, but current transition temperatures require cooling. New “colossal” magnetoresistive materials developed for magnetoresistive heads have an unusually large thermal response near room temperature, as shown in Figure 3 (Venkatesan et al., University of Maryland). This material (LCMO - Lanthanum Calcium Manganese Oxide) shows a dimensionless temperature coefficient of resistance $\alpha \sim 40$ at $T = 275$ K. At present the $1/f$ noise level in this material is too high to be useful in detectors, but reductions in noise through better processing may lead to improved sensors.

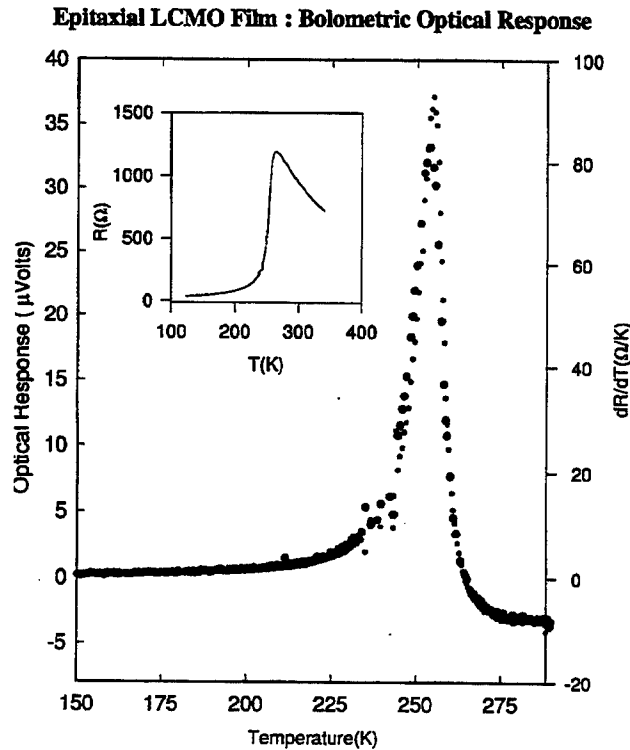


Figure 3: Resistive transition in colossal magnetoresistance material LCMO (Lanthanum Calcium Manganese Oxide) (T. Venkatesan, R. Ramesh and M. Rajeswari, University of Maryland).

LWIR infrared cameras based on uncooled microbolometer arrays are now commercially available from a number of companies including Santa

Barbara Research Center (SBRC) and Texas Instruments. The performance of the SBRC camera is representative of the better units – it is based on a uncooled resistive 320×240 pixel microbolometer array with response in the LWIR band (7 to $13.5 \mu\text{m}$). The sensitivity of the pixels in the array (NETD ~ 50 mK with $f/1.0$ optics) and the uniformity of the array are both very good. The subjective quality of video images taken with the camera is high, better than first generation HgCdTe imagers, and one expects that uncooled LWIR cameras will be useful for a wide range of imaging applications.

Improvements in uncooled microbolometer arrays are underway in a number of areas. Higher responsivity is possible using crystalline VO_x instead of disordered VO_x in resistive bolometers, and possibly through the use of colossal magnetoresistive materials. Better thermal isolation of the pixels can be achieved through narrower and longer pixel ‘legs’ leading to larger thermal response and lower noise. The ultimate limit is determined by black-body thermal coupling between the pixel and its environment. Larger arrays (640×480 and above) with smaller pixels ($25 \times 25 \mu\text{m}^2$) are under development to increase the number of pixels on target. The combination of better responsivity and better thermal isolation should give improved sensitivity NETD ~ 20 to 30 mK. Improved readout IC’s can give lower noise and better uniformity. Power consumption is an important issue for uncooled cameras, because they are inherently portable, and could be widely used in the field. The focal plane array consumes ~ 300 mW, while the rest of the electronics and display take 5 W to 10 W. Lower power operation should be possible through the use of low power electronics. Low cost cameras are also under development. The current price $\$10\text{k}$ to $\$20\text{k}$ could fall to $\sim \$1\text{k}$ if large volume orders are placed for mass market applications such as those in the automotive industry. A large fraction of the cost and weight of current uncooled cameras is associated with the Ge lens. Reflective optics based on metal coated precision molded plastics could lead to large cost and weight reductions.

In summary, uncooled LWIR cameras are becoming increasingly competitive with HgCdTe cameras for a wide range of applications. The attractive qualities of portability and low cost could lead to uncooled cameras dominating the market for LWIR cameras, leaving only the high end to HgCdTe devices. Once uncooled cameras are widely available internationally, one should no longer assume that an adversary lacks good night vision equipment.

4 QUANTUM WELL INFRARED PHOTODETECTORS

Quantum well infrared photodetectors (QWIPs) are man-made extrinsic photoconductors in which quantum wells replace impurity atoms. In a conventional extrinsic photoconductor, free carriers excited from dopant atoms by infrared light provide the signal; in QWIPs, free carriers excited from doped quantum wells provide the signal. The ability to vary the binding energy of electrons in QWIPs to match the desired IR response by changing quantum well depth and width is an important advantage. Most QWIP devices are made from GaAs/AlGaAs heterostructures grown by molecular beam epitaxy (MBE) or metal organic chemical vapor deposition (MOCVD).

Figure 4 is a schematic diagram of a multiple quantum well QWIP device. The well depth and the widths of the wells and barriers are adjusted so that the ground state of electrons in the well is bound and the first excited

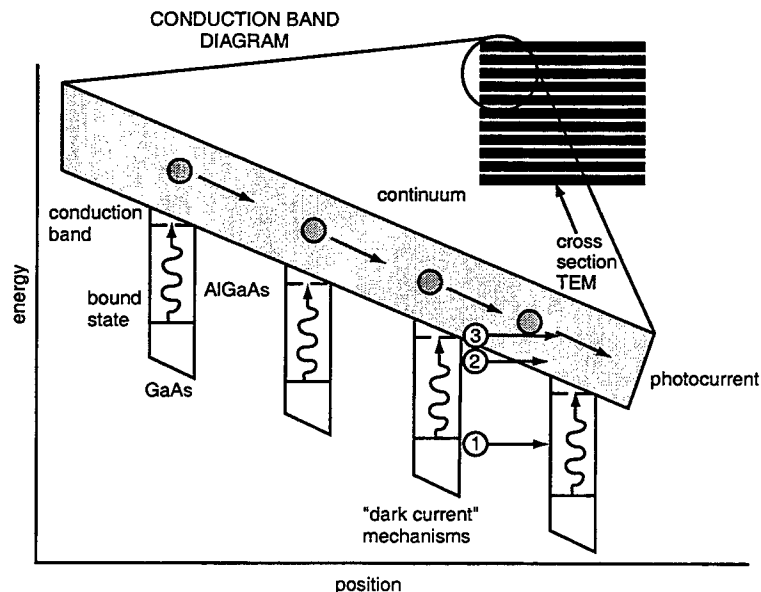


Figure 4: Schematic diagram showing the principle of operation of quantum well infrared photodetector (QWIP) devices with inset of scanned electron microscope photograph of GaAs/AlGaAs heterostructure.

state lies near the top of the well as indicated. The excited states overlap significantly between wells and form the analog of a conduction band in extrinsic semiconductors. Absorbed infrared photons promote electrons from the bound state to the conduction band where they are swept away by an applied electric field to produce the photocurrent.

The fundamental advantage of QWIP devices is the ability to tailor their infrared response, and they are naturally suited to the fabrication of multi-color sensors. QWIPs based on GaAs/AlGaAs heterostructures also benefit from the high quality and uniformity of these semiconductor structures, which are made using a mature technology. As discussed below, QWIP devices are quite sensitive to the polarization of infrared photons and are natural candidates for polarization sensitive sensors.

The primary disadvantages of QWIP devices are low quantum efficiency and low operating temperature. Quantum efficiency is limited by a number of factors. Because each well contains few electrons compared with intrinsic material and absorbs infrared radiation only weakly, a stack of many (typically ~ 100) quantum wells is required in order to obtain sufficient absorption. In addition, the photoconductive gain (see Appendix B.2) of QWIPs is limited to values less than unity by the fact that free carriers are recaptured before travelling the full width of the stack. Quantum mechanical selection rules limit infrared absorption to radiation with electric field polarized perpendicular to the quantum well. An optical coupling structure (see below) is required to rotate the polarization of incoming radiation into the correct orientation for absorption.

At sufficiently low temperatures QWIPs can give excellent sensitivity. However, the required operating temperatures, ~ 70 K and below, are low relative to those for intrinsic photoconductors and bolometers. As described in Appendix B.2, extrinsic photoconductors require relatively low operating temperature for fundamental reasons. Thermal ionization of carriers bound

in dopant atoms (or quantum wells) occurs at temperatures $k_B T$ well below the binding energy (and infrared photon energy), because the entropy of free carriers is much greater. This effect is compounded by the fact that the infrared induced charge carrier density – the signal – is limited by short free carrier lifetimes in QWIP devices. Free-to-bound transitions in quantum wells are very rapid due to the nesting of electron subbands in momentum space with free carrier lifetimes typically $\tau \sim 10$ ps, whereas the minority carrier lifetime in HgCdTe materials is much longer, typically $\tau \sim 1\mu\text{s}$. Miniature coolers which reach the required temperatures are available, but the added stress limits their lifetime to ~ 2000 hours.

Optical couplers are required for all QWIP devices, because quantum well transitions are only excited by electric fields perpendicular to the plane of the well. A coupler is needed to bend the infrared rays and rotate the polarization. Two examples of optical couplers are shown in Figure 5: a corrugated QWIP developed by Princeton University and the Army Research Laboratory (ARL) and a pseudorandom coupler developed at the Jet Propulsion Laboratory (JPL). The corrugated QWIP relies on total internal reflection:

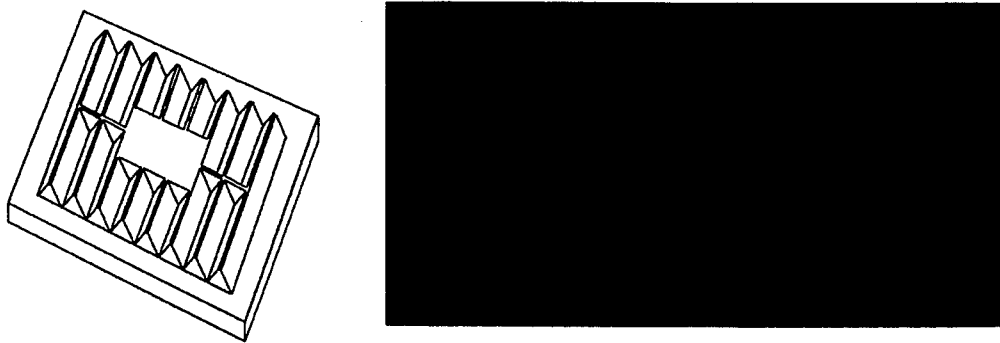


Figure 5: Optical couplers for QWIP devices: (left) corrugated QWIP developed by Princeton University and Army Research Laboratory; (right) pseudorandom coupler developed by the Jet Propulsion Laboratory.

infrared radiation incident from the bottom is trapped by the corrugations

on the top of the device, and its polarization is rotated. The parallel roof shaped structure shown is polarization sensitive with an extinction ratio ~ 4 . In order to avoid polarization sensitivity, JPL has built couplers with pseudorandom corrugations as shown in Figure 5. The complex pattern rotates incident rays to minimize sensitivity to polarization.

QWIP cameras have been developed by a number of makers. Although the requirement for a cooler tends to increase size, weight and cost, JPL has developed miniature hand-held QWIP cameras with very good performance. Lockheed Martin has demonstrated a video camera using a 256×256 pixel QWIP device operating at 60 K. With $f/1.7$ optics and a $2.27^\circ \times 2.27^\circ$ field of view this camera achieves a NETD varying from ~ 7 mK to 35 mK with spatial frequency. The subjective quality of the images is excellent, due in large part to the high spatial uniformity of the array.

An important advantage of QWIP devices is that they are based on a mature GaAs/AlGaAs technology which produces high quality material and permits the growth of complex layered structures. As a result, the uniformity of QWIP devices is very high, and their performance approaches theoretical limits. Their primary disadvantages are low quantum efficiency, and the need for cooling to relatively low temperatures. Consequently their sensitivity is limited. Nonetheless the subjective quality of QWIP images can be much better than that for other infrared cameras with higher sensitivity but lower uniformity. The trade-off between sensitivity and uniformity is an interesting issue for pattern recognition, as described above. Despite an uncertain past, polarization of infrared radiation may prove to be a useful discriminant for recognition of metal targets in organic clutter. QWIP detector arrays are natural candidates for this application. QWIP detector arrays are also naturally suited to "multi-color" infrared detectors arrays, because their wavelength sensitivity can be continuously adjusted during growth.

5 HgCdTe PHOTODETECTOR ARRAYS

HgCdTe photodetectors have fundamental advantages for infrared sensors (detailed in Appendix B.2). Because they are intrinsic photoconductors in which infrared photons excite transitions from the valence to the conduction band, they have high quantum efficiency and low thermally excited carrier density (relative to extrinsic photoconductors). Their band gap can be adjusted by varying the relative proportion of Hg and Cd to produce peak sensitivity from the LWIR through the MWIR bands. These fundamental advantages have led to a considerable investment in HgCdTe technology over the years. However, the actual performance of LWIR HgCdTe detectors has not reached these fundamental limits for a variety of quite technical reasons. For alloys appropriate to the LWIR band, HgCdTe is not highly stable, and the quality of devices is very sensitive to the details of the fabrication process.

An important development between this JASON study and the previous one is the production of large LWIR staring arrays made from HgCdTe. Both Santa Barbara Research Center and Texas Instruments have produced arrays of size 256×256 pixels and 640×480 pixels which give excellent image quality. Reliability has been improved by providing strain relief in the connections between the HgCdTe array and the Si readout integrated circuit (ROIC). SBRC attacks this problem by backing the Si readout with proprietary materials to match the thermal expansion of the HgCdTe array. Texas Instruments epoxies thinned HgCdTe arrays to Si readout ICs so that the differential strain is taken up by the HgCdTe array.

These new HgCdTe LWIR staring arrays provide excellent sensitivity along with high spatial resolution, and they are natural choices for infrared telescopes for which atmospheric absorption, and scattering and absorption by dust and aerosols is an issue. Once infrared capability becomes common, HgCdTe arrays will provide better sensitivity than uncooled bolometer arrays

or QWIPs. However, the market for high performance HgCdTe arrays is small, and it seems that their price will remain high, especially compared with uncooled detector arrays. There is a significant economic issue as to who will pay to bring large HgCdTe arrays into production.

6 DEVELOPMENTS

This section describes a variety of developments which are not limited to any one detector type: 'two color' infrared imagers, improved readout integrated circuits, improved strain relief, and improved materials for thermoelectric coolers.

The use of 'color' in infrared images – the presentation of multiple wavelength bands in one image – promises to improve discrimination of objects just as it does at visible wavelengths. Different materials have different emissivity, and many materials have characteristic absorption features in the LWIR and MWIR bands. Comparison of LWIR and MWIR emission can also improve the accuracy of inferred temperatures. The complexity of multiple color infrared imagers using separate detector arrays for different 'colors' has limited their application in the past.

Infrared detector arrays in which two colors are integrated in a single pixel are under development for QWIP and HgCdTe technologies. Both are well suited to multiple color detectors, because their peak sensitivity can be adjusted. In principle, two color bolometer arrays could also be fabricated by using wavelength selective coatings. Figure 6 illustrates two approaches to the fabrication of two-color pixels.

In a QWIP device the wavelength sensitivity can be changed by adjusting the quantum well depth and/or width during growth of the GaAs/AlGaAs heterostructure. Figure 6 (top) illustrates a two color detector pixel in which two QWIP photoconductors are grown in series. Selective patterning and etching techniques are used to contact the two detectors separately as indicated. For a HgCdTe device the wavelength sensitivity is adjusted by changing the alloy concentrations. Figure 6 (bottom) shows a heterojunction pixel that provides simultaneous MWIR and LWIR sensitivity.

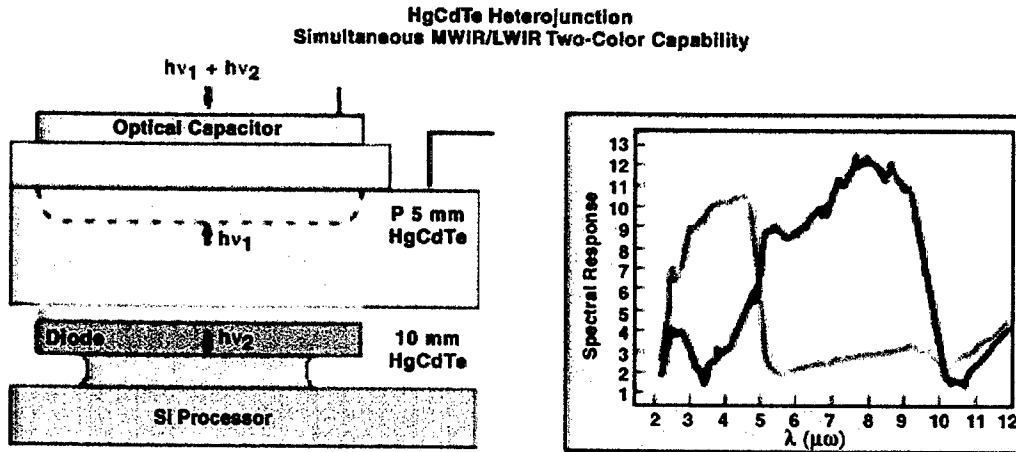
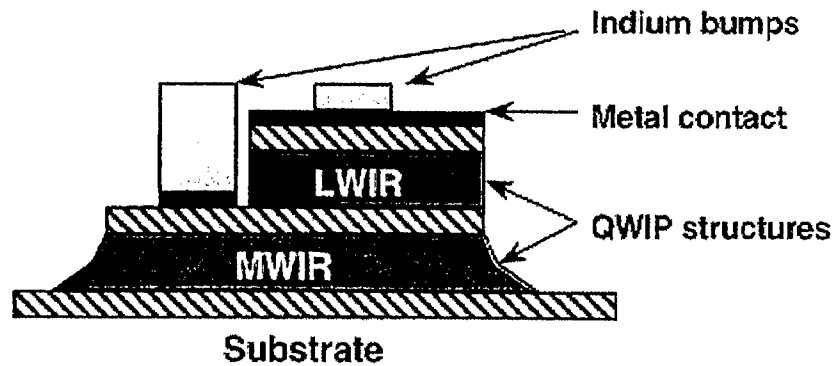


Figure 6: Two color infrared detector pixels: (top) QWIP two color pixel consisting of stacked MWIR and LWIR multiple quantum wells grown in a single GaAs/AlGaAs heterostructure; (bottom) HgCdTe heterojunction detector providing simultaneous MWIR and LWIR band two color capability with spectral response shown.

Readout integrated circuits (ROICs) have improved significantly over the past five years. Silicon CMOS circuitry has generally replaced silicon charged coupled devices (CCDs) enabling the infrared industry to use standard foundry facilities. The use of CMOS lowers cost and enables the design of higher capability readouts. Current CMOS designs typically place the amplifier front end and a switch under each pixel. A row of preamps and analog-to-digital converters (ADCs) is placed along one side of the chip, and the array is read out by sweeping the active pixels. Unless suitable integration can be placed under each pixel, this multiplexing technique reduces the signal-to-noise ratio due to inefficient time averaging. Economic factors often limit infrared detector array developers to the use of old CMOS processes and relatively small wafer sizes.

Considerable improvement would be possible if current CMOS processing were used for infrared readout ICs. For example, with $0.25\ \mu\text{m}$ CMOS one could place an entire 16-bit ADC under each pixel. With such an arrangement each pixel could be continuously read out for improved signal to noise. One could also place considerable processing power on the readout IC to use for signal processing and feature recognition. The availability of these new capabilities could have substantial implications for new readout IC designs.

The size of current readout ICs limit the size of infrared arrays. For example, a 1000×1000 pixel array with $25 \times 25\ \mu\text{m}^2$ pixels has overall dimensions of $2.5 \times 2.5\ \text{cm}^2$ or $1 \times 1\ \text{in}^2$. This is about the limit of current ROIC technology, but could be improved substantially by using modern processes, to produce arrays with more or larger pixels.

Strain relief is important for the reliability of cooled infrared detector arrays. Differential thermal contraction between the detector array and the

Si readout IC places stress on the interconnects which can lead to premature failure. A variety of approaches have been developed over the past five years to address this issue, as illustrated in Figure 7.

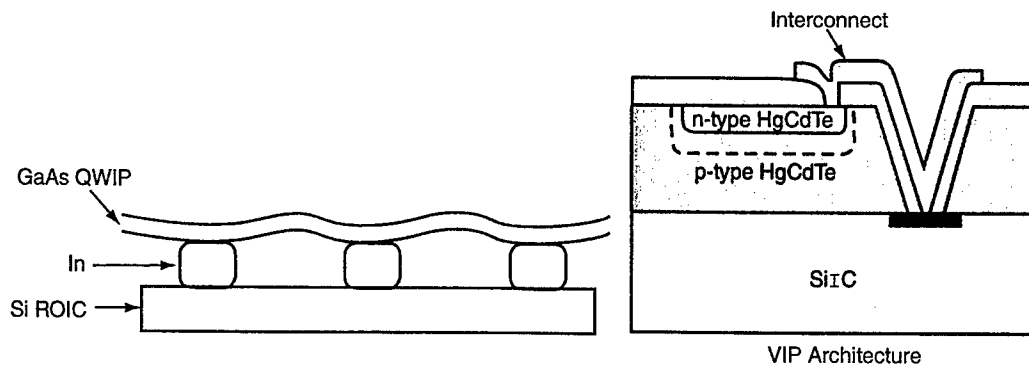


Figure 7: Approaches to thermal strain relief: (left) thinned QWIP arrays indium bump bonded to Si readout IC; (right) thinned HgCdTe array epoxy bonded to Si readout IC.

A FUNDAMENTALS OF INFRARED DETECTOR PERFORMANCE

In this section we briefly discuss fundamental considerations which limit infrared detector performance. Subsection A.1 on blackbody radiation presents the spectrum and noise limits; and Subsection A.2 discusses the physical considerations which determine the detector operating temperature. In both we emphasize simple physical models which can be used to compare different detector types.

A.1 Blackbody Radiation

Spectrum

For detectors of thermal infrared radiation, blackbody radiation is both the source of the signal and an important source of noise. The spectrum of blackbody radiation is easily derived from the statistics of photons in equilibrium with a blackbody of temperature T . The volume density of photons $dN_\gamma/d\lambda$ per wavelength interval $d\lambda$ is simply the product of the density of photon states $8\pi/\lambda^4$ and the average occupation of each state $n(hc/\lambda) = 1/[\exp(hc/\lambda k_B T) - 1]$, the Bose-Einstein distribution function:

$$\frac{dN_\gamma}{d\lambda} = \left(\frac{8\pi}{\lambda^4}\right) \frac{1}{e^{hc/\lambda k_B T} - 1}, \quad (\text{A-1})$$

where hc/λ is the photon energy, with h Planck's constant and c the velocity of light, and k_B is Boltzmann's constant.

The blackbody photon flux $dI_\gamma/d\lambda$ incident on one side of a flat detector of area A collected from a solid angle Ω symmetric about the direction perpendicular to the detector is:

$$\frac{dI_\gamma}{d\lambda} = A \left[\left(\frac{\Omega}{\pi}\right) - \left(\frac{\Omega}{2\pi}\right)^2 \right] \left(\frac{c}{4}\right) \frac{dN_\gamma}{d\lambda}, \quad (\text{A-2})$$

which reduces to:

$$\frac{dI_\gamma}{d\lambda} = 2\pi A \left[\left(\frac{\Omega}{\pi} \right) - \left(\frac{\Omega}{2\pi} \right)^2 \right] \frac{c}{\lambda^4} \frac{1}{e^{hc/\lambda k_B T} - 1}. \quad (\text{A-3})$$

Plots of blackbody photon flux spectra are shown in Figure A-1 for a series of temperatures $T = 240\text{K}$ to 340K assuming a solid angle $\Omega = 2\pi$. As shown, the peak photon flux occurs near $\lambda = 10\mu\text{m}$, and falls off rapidly at shorter wavelengths. In order to detect a blackbody signal from a warm object, one would like to absorb as much of the radiation as possible, and response in the LWIR atmospheric transmission band near $10\mu\text{m}$ is desirable. As shown, the photon flux in the $5\mu\text{m}$ MWIR band is appreciable for temperatures $T > 300\text{K}$, but falls exponentially fast at lower temperatures. This lack of response of MWIR detectors below $T \sim 300\text{K}$ can cause difficulties in imaging relatively cool objects and backgrounds.

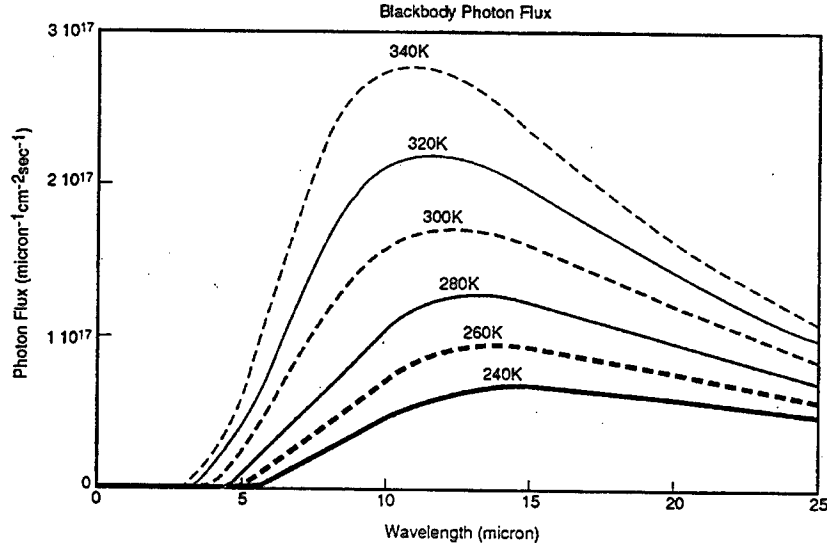


Figure A-1: Blackbody photon flux vs. wavelength at various temperatures indicated (see text)

Fluctuations in Photon Flux

Photons are continually emitted and absorbed by a blackbody, leading to thermal fluctuations δn in the occupation $n(hc/\lambda)$ of each quantum state of the photon gas according to Boson statistics:

$$\langle \delta n^2 \rangle = n(1 + n). \quad (\text{A-4})$$

Near the peak of the blackbody spectrum, the occupation $n < 1$, the photon gas is nondegenerate, and the fluctuations $\langle \delta n^2 \rangle \cong n$ obey simple counting statistics. At longer wavelengths ($\lambda \gg 50\mu\text{m}$ for $T = 300\text{K}$) the photon gas becomes degenerate ($n > 1$) and fluctuations in occupation are much larger $\langle \delta n^2 \rangle \cong n^2$; this regime corresponds to fluctuating speckle patterns with a high degree of coherence.

The total number of photons which arrive at a detector over an integration time Δt is:

$$N_\gamma = \frac{dI_\gamma}{d\lambda} \Delta\lambda \Delta t, \quad (\text{A-5})$$

where $\Delta\lambda$ is the wavelength interval detected. Assuming that the photon gas is nondegenerate at the wavelengths of interest, the fluctuations δN_γ in number of photons are given by:

$$\langle \delta N_\gamma^2 \rangle = N_\gamma. \quad (\text{A-6})$$

These fluctuations correspond to shot noise in the arrival rate I_γ of photons. For a given bandwidth Δf in Hz, fluctuations in the photon current at frequencies much lower than the arrival rate are given by:

$$\langle \delta I_\gamma^2 \rangle = 2I_\gamma \Delta f. \quad (\text{A-7})$$

Generation-Recombination Noise

Now we consider the effect of the incident photon flux on an infrared detector, which we take to be a photoconductor. Each incident photon creates a photoexcited carrier with probability η , the quantum efficiency. For

simplicity we assume that only one type of excited carrier (electrons or holes) is mobile. After creation, the photoexcited carrier drifts in the electric field applied between the contacts of the detector for a distance before it recombines. In doing so, it transfers a charge $q = (\tau_o/\tau_t)e$ between the contacts and through the external circuit, where τ_o is the carrier lifetime, τ_t is the transit time across the full width of the detector, and the ratio $G = (\tau_o/\tau_t)$ is the photoconductive gain. Note that the average transferred charge q is a macroscopic quantity which can have a continuous range of values from $q < e$ to $q > e$ determined by the photoconductive gain (see below). The total number of carriers transferred to the external circuit in a time interval Δt is:

$$N = \eta G N_\gamma, \quad (\text{A-8})$$

with corresponding photocurrent:

$$I = \eta G I_\gamma. \quad (\text{A-9})$$

Blackbody radiation incident on a photoconductor creates carriers according to the process described above. Fluctuations in the number of charges transferred to the circuit in a time Δt are determined by the statistics of carrier generation and recombination, as well as fluctuations in the photon flux:

$$\langle \frac{\delta N^2}{N^2} \rangle = \langle \frac{\delta \eta^2}{\eta^2} \rangle + \langle \frac{\delta G^2}{G^2} \rangle + \langle \frac{\delta N_\gamma^2}{N_\gamma^2} \rangle. \quad (\text{A-10})$$

Here $\langle \delta \eta^2 \rangle$ and $\langle \delta G^2 \rangle$ are fluctuations in the quantum efficiency η and photoconductive gain G determined by averaging over the arrival of N_γ photons. It is a straightforward exercise in statistics to show that:

$$\langle \delta \eta^2 \rangle = \frac{\eta(1-\eta)}{N_\gamma}, \text{ and } \langle \delta G^2 \rangle = \frac{G^2}{\eta N_\gamma}. \quad (\text{A-11})$$

Combining Equations (A-6), (A-10), and (A-11) we find:

$$\langle \frac{\delta N^2}{N^2} \rangle = \frac{(1-\eta)}{\eta N_\gamma} + \frac{1}{\eta N_\gamma} + \frac{1}{N_\gamma} = \frac{2}{\eta N_\gamma}. \quad (\text{A-12})$$

Thus fluctuations $\langle \delta N^2 \rangle / N^2$ in the number of carriers transferred to the external circuit are determined by the number ηN_γ of photoexcited carriers, and are independent of the value G of the photoconductive gain. The factor of 2 in Equation (A-13) arises because both the generation and recombination of photocarriers produce statistical noise. The photoconductive gain G does not introduce additional noise, but acts in the same way as amplifier gain. The corresponding generation-recombination noise current in the external circuit at frequencies $f \ll 1/2\pi\tau_o$ is:

$$\langle \delta I^2 \rangle = 4eIG\Delta f. \quad (\text{A-13})$$

We assume for the moment that the thermal generation of carriers is negligible, so that I in Equation (A-13) is the photocurrent produced by blackbody background radiation. In photodiodes, no statistical noise is produced by recombination, because excited photocarriers are swept out of the active region of the device before they recombine; for this case $G = 1$ and the noise $\langle \delta I^2 \rangle$ is a factor of two smaller than for Equation (A-13). As for quantum detectors, bolometers are also ultimately limited by photon shot noise, although this limit is not commonly approached in practice.

The fundamental limit to the performance of an ideal infrared detector is given by the generation-recombination noise associated with background blackbody radiation. This limit is usually expressed in terms of the noise equivalent photon power (NEP) incident on the detector:

$$NEP = \left(\frac{hc}{\lambda} \right) \frac{1}{e\eta G} \langle \delta I^2 \rangle^{1/2}. \quad (\text{A-14})$$

Inserting the blackbody photocurrent fluctuations $\langle \delta I^2 \rangle$ due to generation-recombination noise in photoconductors from Equation (A-13) we find:

$$NEP = \left(\frac{hc}{\lambda} \right) \left\{ \left(\frac{8\pi A\Delta f}{\eta} \right) \left[\left(\frac{\Omega}{\pi} \right) - \left(\frac{\Omega}{2\pi} \right)^2 \right] \left(\frac{c\Delta\lambda}{\lambda^4} \right) \frac{1}{e^{hc/\lambda k_B T} - 1} \right\}^{1/2}. \quad (\text{A-15})$$

For photodiodes the noise equivalent power due to photon shot noise is smaller than Equation (A-15) by a factor $1/\sqrt{2}$. These expressions are valid

only for $hc/\lambda k_B T > 1$, because we have assumed that the photon gas is non-degenerate (incoherent). This assumption is justified near the peak of the blackbody spectrum and at shorter wavelengths. For blackbody sources the signal-to-noise ratio is:

$$S/N = \frac{(hc/\lambda)I_\gamma}{NEP}. \quad (\text{A-16})$$

where I_γ is the blackbody photon current from Equation (A-3). Combining expressions we find for photoconductors:

$$S/N = \left\{ \left(\frac{\pi\eta A}{2\Delta f} \right) \left[\left(\frac{\Omega}{\pi} \right) - \left(\frac{\Omega}{2\pi} \right)^2 \right] \left(\frac{c\Delta\lambda}{\lambda^4} \right) \frac{1}{e^{hc/\lambda k_B T} - 1} \right\}^{1/2}. \quad (\text{A-17})$$

For photodiodes the signal-to-noise ratio due to photon shot noise is larger than Equation(A-17) by a factor $\sqrt{2}$. The signal-to-noise ratio is maximized for thermal blackbody sources by maximizing the number of detected blackbody photons through increases in detector area A , solid angle Ω , spectral width $\Delta\lambda$, and the quantum efficiency η , and operation at wavelengths λ near the peak of the blackbody photon flux spectrum, shown in Figure A-1. Except for increasing the quantum efficiency η , these trends also increase the NEP and would be undesirable for non-thermal sources.

Another standard measure of infrared noise performance is the specific detectivity:

$$D^* = \left(\frac{A^{1/2}\Delta f^{1/2}}{NEP} \right). \quad (\text{A-18})$$

The background-limited infrared performance (BLIP) limit from Equation (A-15) for photoconductors is:

$$D^* = \left(\frac{\lambda^3}{hc} \right) \left\{ \left(\frac{\eta}{8\pi c\Delta\lambda} \right) \left[\left(\frac{\Omega}{\pi} \right) - \left(\frac{\Omega}{2\pi} \right)^2 \right]^{-1} \left(e^{hc/\lambda k_B T} - 1 \right) \right\}^{1/2}. \quad (\text{A-19})$$

For photodiodes the specific detectivity D^* due to photon shot noise is larger than Equation(A-19) by a factor $\sqrt{2}$. For $T = 300\text{K}$, $\Omega = 2\pi$, $\eta = 1$, $\lambda = 10\mu\text{m}$, and $\Delta\lambda = 1\mu\text{m}$, the BLIP detectivity for photoconductors from Equation (A-19) is

$$D^* = 6.43 \times 10^{10} \text{cmHz}^{1/2}/W. \quad (\text{A-20})$$

Note that the use of the specific detectivity D^* to characterize detectors of thermal sources can be misleading, because lower NEP is not always equivalent to higher signal to noise ratio, as discussed above. For example, detectors which have smaller solid angles Ω or do not respond at wavelengths near the peak in the blackbody spectrum can have higher detectivity than Equation (A-20), but have lower signal-to-noise ratios for thermal sources, because they detect fewer photons.

A measure of noise performance of detector systems is the noise-equivalent temperature difference (NETD), approximately the smallest temperature change which can be detected in a source of thermal radiation. The NETD is particularly useful, because it includes the influence of all relevant parameters and is an unambiguous measure of the performance of a given system. The NETD is defined as the temperature difference of a blackbody source at a specified temperature (e.g. $T = 300$ K) which corresponds to the same change in detected signal as the system noise.

A.2 Temperature of Operation

Most infrared detectors with sensitivity in the LWIR band require cooling in order to reduce the number of thermally excited carriers. The temperature of operation required for a certain level of performance is a critical parameter, because the cooling system often dominates the size, weight and reliability of the detector system. Temperatures above the 77K boiling point of liquid nitrogen are desirable, because they can be reached using nitrogen-based coolers which are standard in many applications. Lower temperatures can be reached using other gases, at the expense of greater weight and non-standard operation.

The specific factors which determine the temperature of operation for a given detector system are complex, and it is not always easy to compare

the promise of different approaches. In this section we discuss the physical processes which determine operation temperature from a general point of view, and present a number of simple models. Our goal is to obtain an approximate picture which is valid for a range of detector designs, rather than a detailed description of any given detector.

Quantum Detectors

Generation-recombination (G-R) noise associated with the production of thermally-excited carriers sets the fundamental limit to quantum detector performance, as discussed above in Section 2. As the detector is cooled, the G-R noise level decreases as the square root of the thermally-generated carrier density n_{th} , and the signal-to-noise ratio increases proportionately. The physical quantity which determines the signal-to-noise ratio is the ratio n_s/n_{th} of the carrier concentration n_s produced by the infrared signal to the thermally-generated concentration n_{th} . A primary goal in detector design is to increase this ratio as much as possible.

In this subsection we consider the statistics of carrier generation and recombination in order to develop principles for the design of infrared detectors with high operation temperatures. Using simple models, we show that the operating temperature is maximized by maximizing the radiative efficiency of the carriers generated by infrared radiation, by matching the density of levels between which radiative transitions take place. It is well known that matching the absorption spectrum of the detector to the source of radiation also maximizes operating temperature by reducing the thermal generation rate associated with states which absorb blackbody radiation but are not excited by the signal.

For simplicity we consider a two-level model of a quantum detector. The lower level represents the ground state of electrons in the system, and is assumed to be heavily populated at low temperatures; specific examples are a donor level for an extrinsic photoconductor, or a bound state in a quantum

well. The upper level represents the excited states of the system which are assumed to be unpopulated at sufficiently low temperatures; specific examples are the conduction bands of extrinsic photoconductors, or of quantum well detectors. We assume that only excited carriers are mobile and contribute to the detected signal; the free carrier concentration is labelled n and we refer to these as electrons. The volume density of quantum states in the lower level is labelled N_1 and that in the upper level N_2 . We assume that a fraction of the lower states with density N_0 are empty even at very low temperatures due to the presence of occupied traps which remove carriers from the system. For example, an n-type extrinsic photoconductor with donor and acceptor concentrations N_D and N_A would have $N_0 = N_A$, $N_1 = N_D$, and $N_2 = N_C$, where N_C is the effective density of states in the conduction band, given below.

Radiative Efficiency

For the ideal case in which all transitions between levels 1 and 2 occur via radiative processes, the rate of change of the electron density n is given by:

$$\frac{dn}{dt} = (J_t \sigma_{ar} + J_s \sigma_{ar})(N_1 - N_0 - n) - nv \sigma_{cr}(N_0 + n). \quad (\text{A-21})$$

For this case thermal equilibrium is established via the absorption and emission of blackbody radiation at the detector temperature T , and no other thermalization processes are active. The first thermal generation term is the rate via the absorption of blackbody radiation, for which J_r is the blackbody radiation flux and σ_{ar} is the radiative absorption cross section. The second generation term in Equation(A-21) is the rate via absorption of the infrared signal with photon flux J_s ; the absorption cross section for the signal is normally the same as for blackbody radiation. The third term in Equation(A-21) describes the radiative recombination of excited carriers with thermal velocity v and capture cross section σ_{cr} . If the density of excited carriers n is much smaller than the trap density N_0 , the rate equation is approximately

linear:

$$\frac{dn}{dt} = (J_t \sigma_{ar} + J_s \sigma_{ar})(N_1 - N_0) - \frac{n}{\tau_r} \quad (\text{A-22})$$

where $\tau_r = 1/(v \sigma_{cr} N_0)$ is the radiative lifetime of excited carriers. The solutions to Equation (A-22) are simply decaying exponentials with characteristic time τ_r .

In thermal equilibrium with no signal present, the thermal rate of generation of carriers just balances the rate of recombination. This fact can be used to relate the cross sections for radiative absorption and capture. In thermal equilibrium the carrier concentration from Equation (A-22) is:

$$n_t = J_t \sigma_{ar} (N_1 - N_0) \tau_r. \quad (\text{A-23})$$

The thermal carrier concentration n_t can also be found from the statistics of electrons. At low temperatures for which relatively few carriers are excited ($n_t \ll N_0$) we have approximately:

$$n_t = \frac{N_2(N_1 - N_0)}{N_0} e^{-\Delta E/k_B T}. \quad (\text{A-24})$$

Combining Equations (A-23) and (A-24) we find that the radiative cross sections for absorption and capture are proportional:

$$\sigma_{ar} = \left(\frac{1}{J_t \tau_r} \right) \left(\frac{N_2}{N_0} \right) e^{-\Delta E/k_B T} = \sigma_{cr} \left(\frac{v N_2}{J_t} \right) e^{-\Delta E/k_B T}. \quad (\text{A-25})$$

The apparent exponential temperature dependence of σ_{ar} in Equation (A-25) is cancelled by that of the blackbody flux J_t , and the cross section is independent of the trap density N_0 as is required.

For the ideal case in which all transitions are radiative, the ratio n_s/n_t of the signal to the thermally-generated carrier concentration from Equation (A-22) is simply:

$$\frac{n_s}{n_t} = \frac{J_s}{J_t}. \quad (\text{A-26})$$

Thus the flux of infrared photons from the signal must be sufficiently large compared with that from a blackbody at the detector temperature in order

to obtain good noise performance. However, this ideal case is not always obtained in practice, because thermalization of the carrier distribution often occurs via non-radiative mechanisms such as phonon absorption and emission. For this case we need to add the nonradiative rates of carrier generation and recombination to the rate equation for n :

$$\frac{dn}{dt} = (J_t\sigma_{ar} + J_s\sigma_{ar} + A_{nr})(N_1 - N_0) - n\left(\frac{1}{\tau_r} + \frac{1}{\tau_{nr}}\right) \quad (\text{A-27})$$

where A_{nr} describes the nonradiative generation of carriers and τ_{nr} is the nonradiative lifetime. These nonradiative rates are often much faster than the radiative terms, and dominate the thermalization of excited carriers in the detector. In this case, illumination by the signal produces a smaller increase in carrier concentration n_s and the signal to noise ratio is reduced.

We can use the principle of detailed balance to find the ratio n_s/n_t of the signal to the thermally-generated carrier concentration including nonradiative effects. From Equation (A-27) we find:

$$n_s = J_s\sigma_{ar}(N_1 - N_0)\tau_{tot} \quad (\text{A-28})$$

where τ_{tot} is the total lifetime including both radiative and nonradiative processes:

$$\frac{1}{\tau_{tot}} = \frac{1}{\tau_r} + \frac{1}{\tau_{nr}}. \quad (\text{A-29})$$

In the present context, the principle of detailed balance states that the radiative processes and the nonradiative processes in Equation (A-27) individually balance in thermal equilibrium. Thus the rates of radiative generation and recombination are unchanged by the addition of the nonradiative process, and Equation (A-23) for the thermal carrier concentration remains valid.

Thus for the general case including both radiative and nonradiative thermalization of carriers, the ratio n_s/n_t of the signal to the thermally-generated carrier concentration is:

$$\frac{n_s}{n_t} = \left(\frac{J_s}{J_t}\right) \left(\frac{\tau_o}{\tau_r}\right) \quad (\text{A-30})$$

where τ_o/τ_r is the quantum efficiency for the radiative recombination of excited carriers, and J_t is the flux of blackbody radiation from a source at the same temperature as the detector. This expression is very useful, because it allows us to compare different approaches to detector design. Equation (A-30) tells us that the highest signal-to-noise ratio at a given temperature, and thus the highest operating temperatures, are obtained from detectors with the highest radiative efficiency. Designs such as extrinsic photoconductors and quantum well detectors, for which the capture of excited carriers can proceed via phonon emission, often require lower operating temperatures to compensate for greater nonradiative rates. The absolute value of the lifetime does not directly influence the operating temperature. In fact shorter radiative lifetimes are desirable, because they correspond to stronger absorption and permit the construction of smaller pixels. Kinch and Yariv have used a similar approach to study the effect of lifetime on operating temperature for quantum well detectors as discussed below.

Entropy Ionization

If the density of excited states in an infrared photodetector is much larger than the density of ground states, the ground states thermally depopulate at a lower temperature than one might expect from a simple Boltzmann factor argument. This “entropy ionization” can have an important influence on the operating temperature of quantum detectors. For our simple two-level model, the volume density of states N_2 for the upper level corresponds to the effective density of states in the conduction band $N_2 = N_C$:

$$N_C = 2n_{\min} \left(\frac{2\pi m_e k_B T}{h^2} \right)^{3/2} \quad (\text{A-31})$$

where n_{\min} is the number of conduction band minima, and m_e is the electron density of states effective mass. The effective density of states can be quite large; for example, with $n_{\min} = 1$, $m_e = 0.1m_o$ and $T = 100\text{K}$, we find $N_C = 1.5 \times 10^{17} \text{ cm}^{-3}$. For extrinsic photoconductors, the lower level in our model corresponds to donors states with density $N_1 = N_D$, and the traps

are compensating acceptors with density $N_0 = N_A$. Depending on the type and design of the detector, the relative density of levels N_0 , N_1 , and N_2 vary by orders of magnitude, and have a large influence on the required operating temperature.

At low temperatures the occupation of the upper level is small; the thermal carrier density is nondegenerate and given by Maxwell-Boltzmann statistics:

$$n_t = N_2 e^{-(E_2 - \mu)/k_B T} \quad (\text{A-32})$$

where μ is the chemical potential (Fermi level). The density of electrons n_1 in the lower level is degenerate and given by Fermi-Dirac statistics:

$$n_1 = N_1 \frac{1}{e^{(E_1 - \mu)/k_B T} + 1}. \quad (\text{A-33})$$

The total carrier concentration is fixed and equal to the density N_1 of lower levels minus the density N_0 of traps. Setting $n_t + n_1 = N_1 - N_0$ we obtain a quadratic equation for the chemical potential, and thus the thermal carrier concentration n_t . At temperatures sufficiently low that the carrier concentration is small compared with the trap density $n_t \ll N_0$ the solution of this quadratic equation yields approximately:

$$n_t = (N_1 - N_0) \left(\frac{N_2}{N_0} \right) e^{-\Delta E/k_B T} \quad (\text{A-34})$$

the same as Equation (A-24) above. Thus the density of thermally-excited carriers n_t is equal to the total electron density $(N_1 - N_0)$ multiplied by a Boltzmann factor containing the energy difference $\Delta E = E_2 - E_1$ between the upper and lower levels, weighted by the relative densities N_2/N_0 of the upper level and traps.

It is convenient to write Equation (A-34) in terms of the change in Helmholtz free energy per electron $\Delta F = \Delta E - T\Delta S$ between the upper and lower levels, where ΔS is the difference in entropy per electron between the upper and lower levels. The entropy per particle is approximately the logarithm of the number of available states: N_2 for the upper level which is

nearly empty, and N_0 for the lower level which is partially full, and we have approximately:

$$\Delta F = \Delta E - k_B T \ln \left(\frac{N_2}{N_0} \right). \quad (\text{A-35})$$

Using the free energy difference, the thermally-excited carrier density takes the simple form:

$$n_t = (N_1 - N_0) e^{-\Delta F/k_B T}. \quad (\text{A-36})$$

That is: the thermally-excited carrier concentration is just the product of the total concentration of electrons and a Boltzmann factor with the change in free energy ΔF taking the place of the change in energy ΔE . This use of the Helmholtz free energy to represent the internal degrees of freedom is standard in statistical physics, and very convenient when treating the relative occupation of levels with different degeneracies.

If the density of upper states is larger than the density of lower states, carriers gain entropy on excitation, and the number of excited carriers can be much larger than one might expect. Furthermore, the lower level will depopulate at a lower temperature than predicted by a simple Boltzmann factor argument using the energy difference between levels ΔE . For an extrinsic photoconductor, this depopulation corresponds to ionization of the donor levels. We can estimate the ionization temperature T_i by setting $\Delta F/k_B T = 1$ in Equation (A-36):

$$k_B T_i = \frac{\Delta E}{1 + \ln \left(\frac{N_2}{N_0} \right)}. \quad (\text{A-37})$$

Ordinarily N_2 is a function of temperature, so that Equation (A-37) is actually a transcendental equation for T_i . If $N_2/N_0 \gg 1$, as is often the case, we find that the lower levels ionize at temperatures much lower than those corresponding to the energy difference ΔE . For an LWIR detector with $\Delta E = 100$ meV, $N_2 = 10^{17} \text{ cm}^{-3}$, and $N_0 = 10^{15} \text{ cm}^{-3}$, the ionization temperature from Equation (A-19) is $T \sim 180\text{K}$, even though the energy gap corresponds to temperatures $T \sim 1000\text{K}$. Once the carriers ionize, the free carrier concentration becomes temperature independent, and the device is insensitive to

radiation. In order to operate the detector successfully it must be cooled well below the ionization temperature.

The ionization temperature of extrinsic photoconductors can be increased by increasing the trap density N_0 to a significant fraction of the density of lower levels N_2 . Increasing N_0 decreases the thermally-excited carrier density n_{th} (Equation (A-34)) at a given temperature in the freeze-out regime and increases the ionization temperature T_i (Equation (A-37)). The largest increase in ionization temperature is obtained when N_0 approaches N_1 , and a significant fraction of lower states are empty at low temperatures. In general, one can increase the ionization temperature by making N_0 , N_1 , and N_2 all the same order of magnitude, thus reducing the entropy difference between the upper and lower levels. The effect of trap density N_0 on the figure of merit n_s/n_t for noise performance (Equation (A-30)) in the operating regime below the ionization temperature is determined by carrier recombination. Increasing N_0 proportionately decreases the radiative lifetime τ_r and can also change the nonradiative recombination rate. Normally a reduction in lifetime is undesirable, because the change in carrier density n_s due to the signal is reduced. However, if the radiative efficiency is high, the signal and thermal contributions to the carrier concentration are reduced by the same factor, and the ratio n_s/n_t remains approximately unchanged. If non-radiative recombination is important, then the dependence of the radiative efficiency on trap density N_0 determines noise performance. The discussion above assumes that the detector is the primary source of noise in the system. If the detector system is amplifier-noise limited, then the reduction in photoconductive gain associated with a shorter carrier lifetime worsens noise performance.

B APPENDIX: IMAGING BOLOMETER ARRAYS

Bolometers operate by sensing the temperature rise associated with the absorption of radiation. Bolometers are one of the oldest types of radiation detector, and they have many advantages. Bolometers respond to absorbed energy, and can be made sensitive to a very wide range of wavelengths. Because they sense heat rather than photocarriers, bolometers are insensitive to the photocarrier population and dynamics. As a result, bolometers can be made from low-tech materials, and they can be operated at relatively high temperatures. These properties make bolometers well suited to precision measurements of radiant energy. However, conventional bolometers are typically slow and insensitive compared with quantum detectors.

Imaging arrays of small microbolometers have been under development since the 1980s, notably through the HIDAD (High Density Array Development) program by Texas Instruments and by Honeywell. Using modern semiconductor processing techniques, large staring arrays (238×340 pixels) of small ($50 \times 50 \mu\text{m}^2$) bolometer elements were fabricated above, and thermally isolated from, a Si substrate containing readout electronics. The temperature-sensing element used by Texas Instruments is a ferroelectric material, while that used in the Honeywell approach is a resistive thermometer. In the early 1990s the program was declassified. Since then development of uncooled microbolometer arrays has been actively pursued by a number of companies for military and for commercial applications. Santa Barbara Research Center, Lockheed Martin, Infrared Solutions, and Raytheon-Amber are using variants of the Honeywell approach, while Texas Instruments has developed a second generation ferroelectric approach. These bolometer arrays are optimized for thermal radiation in the long-wave infrared (LWIR) atmospheric transmission band. Good noise performance at room temper-

ature has been achieved from both approaches. Typical values of the noise effective temperature difference in 1997 NETD $\simeq 40$ mK to 80 mK for f/1 optics at video frame rates (30 Hz to 60 Hz). The ability of microbolometer arrays to operate at room temperature is a strong advantage over quantum detectors, which must be cooled to ~ 80 K. However, quantum detector arrays made from HgCdTe and InSb achieve better noise performance NETD ~ 10 mK to 20 mK in the mid-wave (MWIR) and long-wave infrared atmospheric transmission bands.

Microbolometer arrays will likely have a major impact on infrared imaging. Their sensitivity and image quality is currently adequate for many applications, and their cost could fall to a small fraction of current LWIR imager prices with quantity production. Bolometers are inherently multi-use devices and could be adapted for use at different wavelengths by changing the absorptive coating. The performance of current microbolometer arrays is not near their fundamental limits, and improvements can be expected with continued development. In this section we discuss factors which currently limit performance and make suggestions for improvements.

B.1 Bolometer Noise

A bolometer consists of a temperature sensing element with heat capacity C , connected to a heat sink through a thermal conductance G . The device senses absorbed radiation via the increase in temperature resulting from the deposited energy. The temperature rise for steady illumination is given by:

$$\Delta T = \frac{P_\gamma}{G} \quad (\text{B-1})$$

where P_γ is the absorbed power. The thermal time constant of the bolometer is:

$$\tau = \frac{C}{G}. \quad (\text{B-2})$$

The bolometer responds to changes in illumination up to the characteristic frequency $f_c = 1/2\pi\tau$, above f_c the response rolls off.

The temperature rise ΔT produced by illumination is typically sensed via a corresponding change in electrical resistance or electric polarization of the bolometer element, and the overall response is proportional to the temperature coefficient of resistance dR/dT or polarization. High temperature coefficients are necessary to overcome electronic noise in the readout electronics and the bolometer itself. The responsivity of bolometers is discussed in detail below.

The fundamental noise limit for bolometers is set by temperature fluctuations in the sensitive element, given by:

$$\langle \delta T^2 \rangle = \frac{k_B T^2}{C} \quad (\text{B-3})$$

where T is the temperature of the bolometer. For a given deposited energy ΔE , the ratio of the rms thermal fluctuation to the temperature rise is:

$$\frac{\langle \delta T^2 \rangle^{1/2}}{\Delta T} = \frac{k_B T}{\Delta E} \left(\frac{C}{k_B} \right)^{1/2}. \quad (\text{B-4})$$

Thus the best energy resolution is obtained with the smallest heat capacity. Small heat capacity also reduces the bolometer time constant and improves the response speed.

It is interesting to relate thermal fluctuation noise to the number of atoms N_a in the sensitive element. Above the Debye temperature T_D of the bolometer material, all of the thermal degrees of freedom are excited, and the heat capacity is $C = 3N_a k_B$ from the principle of equipartition. For this case bolometer noise is proportional to the square root of the number of degrees of freedom:

$$\frac{\langle \delta T^2 \rangle^{1/2}}{\Delta T} = \frac{k_B T}{\Delta E} (3N_a)^{1/2}. \quad (\text{B-5})$$

To reduce temperature fluctuations above the Debye temperature one must reduce the number of atoms in the bolometer element or reduce the temperature. Below the Debye temperature the heat capacity decreases rapidly

as vibrational motion is frozen out, and noise performance improves correspondingly. Thus it is desirable to choose bolometer materials with Debye temperatures larger than the temperature of operation $T_D > T$, if possible. For Si the Debye temperature is $T_D = 645$ K.

The power spectrum of thermal fluctuations in the bolometer element can be found from the autocorrelation function, which decays exponentially in time with the bolometer time constant τ :

$$\langle \delta T(t_o) \delta T(t_o + t) \rangle = \langle \delta T^2 \rangle \exp(-|t|/\tau). \quad (\text{B-6})$$

The power spectrum for temperature fluctuations is proportional to the Fourier transform of the correlation function:

$$S_{\delta T^2}(f) = 2 \int_{-\infty}^{\infty} \langle \delta T(t_o) \delta T(t_o + t) \rangle e^{-i2\pi f t} dt. \quad (\text{B-7})$$

Performing the integral we have:

$$S_{\delta T^2}(f) = \left(\frac{4\tau k_B T^2}{C} \right) \frac{1}{1 + (2\pi f \tau)^2}. \quad (\text{B-8})$$

Below the characteristic frequency $f_c = 1/2\pi\tau$, the power spectrum is frequency independent, and the noise equivalent illumination power due to thermal fluctuations is given by:

$$\langle \delta P_{th}^2 \rangle = \frac{4k_B T^2 G \Delta f}{\eta}. \quad (\text{B-9})$$

where η is the quantum efficiency for absorption of photons. From Equation (B-9) we find that the noise power can be reduced by reducing the thermal conductance G and by reducing the temperature. The heat capacity does not appear in this expression, because the temperature fluctuations are spread over a bandwidth proportional to $1/C$. Combining these results, we find that bolometer noise performance improves as we reduce the heat capacity and thermal conductance. Thus bolometers are natural candidates for microfabrication.

B.2 Comparison of Bolometers with Quantum Detectors

Photon shot noise determines the fundamental background-limited infrared performance (BLIP) for any type of infrared detector. The average fluctuation δP_γ in illumination power incident on the detector due to photon shot noise is:

$$\langle \delta P_\gamma^2 \rangle = 2P_\gamma h\nu \Delta f \quad (\text{B-10})$$

where P_γ is the illumination power and $h\nu$ is the photon energy. The ratio of shot noise to thermal fluctuation noise in a bolometer is:

$$\frac{\langle \delta P_\gamma^2 \rangle}{\langle \delta P_{th}^2 \rangle} = \frac{1}{2} \left(\frac{\Delta T_\gamma}{T} \right) \left(\frac{h\nu}{k_B T} \right) \quad (\text{B-11})$$

where $\Delta T_\gamma = \eta P_\gamma / G$ is the temperature increase produced by illumination. This relation shows that it is difficult to make infrared bolometers which approach background limited performance for low illumination levels for which ΔT_γ is small. Bolometers are well suited to precise measurements of large signals, such as the thermal emission of 300 K blackbodies, and can approach the BLIP limit in this case. For uncooled microbolometers looking at 300 K sources in the LWIR band, $h\nu/k_B T \sim 4$, $\Delta T_\gamma \sim 1$ K (see below), and $\langle \delta P_\gamma^2 \rangle / \langle \delta P_{th}^2 \rangle \sim 0.01$, so that the theoretically detectable temperature difference NETD ~ 10 mK is ~ 10 times larger than the BLIP limit. Cooling and operation in shorter wavelength bands improves performance proportionately. For visible light $h\nu/k_B T \sim 80$ ($T = 300$ K), and uncooled bolometer arrays are theoretically capable of approaching background limited performance $\langle \delta P_\gamma^2 \rangle / \langle \delta P_{th}^2 \rangle \sim 1$ for high levels of illumination such as daytime images of the earth's surface.

The sensitivity and noise performance of bolometers improves as the thermal conductance G decreases. A lower limit to G is determined by thermal coupling to the detector environment via blackbody radiation. From the

Stefan-Boltzmann law we find:

$$G_{BB} = 4\varepsilon\sigma_{SB}T^3A \quad (\text{B-12})$$

where ε and A are the emissivity and area of the bolometer element, and $\sigma_{SB} = \pi^2 k_B^4 / 60 h^3 c^2 = 5.67 \times 10^{-8} \text{ W/m}^2\text{K}^4$ is the Stefan-Boltzmann constant. For HIDAD specifications we find $G_{BB} \simeq 1.5 \times 10^{-8} \text{ W/K}$. The temperature rise ΔT_γ produced by illumination in the radiative coupling limit is:

$$\frac{\Delta T_\gamma}{\Delta T_S} \simeq \frac{1}{4} \left(\frac{\Omega}{\pi} \right) \left(\frac{\varepsilon}{\varepsilon_S} \right) \left(\frac{T_S}{T} \right)^3 \quad (\text{B-13})$$

where Ω is the solid angle through which the detector is illuminated by a source of emissivity ε_S at temperature T_S . For uncooled microbolometer arrays the source and detector temperatures are the same and $\Delta T_\gamma / \Delta T_S = \Omega / 4\pi$, giving $\Delta T_\gamma \sim 20 \text{ K}$ for f/1 optics, which corresponds to a noise effective temperature difference NETD $\sim 4 \text{ mK}$. Cooling reduces the thermal conductance due to radiative coupling dramatically. For example, cooling from room temperature to 80 K reduces G_{BB} by a factor ~ 50 .

We can compare the performance of radiatively coupled bolometers to quantum detectors for wide band blackbody sources by inserting the temperature rise from the previous expression into the ratio of shot to temperature fluctuation noise powers:

$$\frac{\langle \delta P_\gamma^2 \rangle}{\langle \delta P_{th}^2 \rangle} = \frac{1}{8} \left(\frac{\Omega}{\pi} \right) \left(\frac{\varepsilon_S}{\varepsilon} \right) \left(\frac{T_S}{T} \right)^4 \left(\frac{h\bar{\nu}}{k_B T} \right) \quad (\text{B-14})$$

where $h\bar{\nu}$ is the average photon energy for the blackbody source. Doing the average for shot noise distributed over the blackbody spectrum, and assuming nondegenerate statistics, one finds:

$$h\bar{\nu} = \frac{360\zeta(5)}{\pi^4} k_B T \simeq 3.83 k_B T \quad (\text{B-15})$$

where $\zeta(5)$ is the Riemann zeta function for argument 5.

Radiative coupling contributes an additional source of noise, which is

simply the shot noise associated with the absorption and emission of black-body photons at the detector temperature T :

$$\langle \delta P_{BB}^2 \rangle = 4P_{BB}h\nu\Delta f \quad (\text{B-16})$$

where $P_{BB} = A\epsilon\sigma_{SB}T^4$ is the total power radiated by the bolometer element, and $h\nu$ is given above. The numerical factor is 4 instead of 2, because both absorption and emission of photons contribute to the noise. We can assess the importance of this noise source for detectors in which blackbody radiation determines the thermal conductance by taking the ratio of shot noise associated with the signal to temperature fluctuation noise in the radiation coupled limit:

$$\frac{\langle \delta P_\gamma^2 \rangle}{\langle \delta P_{BB}^2 \rangle} = \frac{1}{2} \left(\frac{\Omega}{\pi} \right) \left(\frac{\epsilon_S}{\epsilon} \right) \left(\frac{T_S}{T} \right)^5. \quad (\text{B-17})$$

For equal emissivities and temperatures in uncooled detectors this ratio is $\langle \delta P_\gamma^2 \rangle / \langle \delta P_{BB}^2 \rangle = \Omega/2\pi$, always less than unity ($\sim 1/10$ for f/1 optics), because the solid angle associated with the source is smaller than 2π . Thus for radiatively coupled uncooled bolometers the noise performance cannot reach the BLIP limit. If the detector is cooled, the shot noise associated with radiation coupling falls rapidly, and the BLIP limit is reached at moderate temperatures ($T \sim 200$ K for f/1 optics). Whenever the thermal conductance G exceeds the radiation-coupled limit, conventional thermal fluctuation noise dominates.

B.3 Responsivity

The noise equivalent power δP_γ of an ideal bolometer is given by:

$$\langle \delta P_\gamma^2 \rangle = 4k_B T^2 G \Delta f \quad (\text{B-18})$$

where T is the temperature, G is the thermal conductance to the substrate, and Δf is the bandwidth in Hz. The response ΔR of a resistive bolometer is

proportional to the temperature coefficient dR/dT , which can be expressed in dimensionless form:

$$\alpha = \frac{d \log R}{d \log T} = \left(\frac{T}{R} \right) \frac{dR}{dT}, \quad (\text{B-19})$$

the temperature coefficient α is the slope of a log-log plot of R vs. T . Then the resistance change corresponding to the absorbed power P_γ is:

$$\frac{\Delta R}{R} = \frac{\alpha P_\gamma}{GT}. \quad (\text{B-20})$$

The resistance fluctuations δR due to temperature fluctuations in the bolometer are given by:

$$\left\langle \left(\frac{\delta R}{R} \right)^2 \right\rangle = \frac{4\alpha^2 k_B \Delta f}{G}. \quad (\text{B-21})$$

For temperature fluctuation noise to dominate in a resistive bolometer, it must be larger than Johnson noise. Assuming that a bias current I_B is used to measure the resistance, the ratio of these two noise sources is given by:

$$\frac{I_B^2 \langle \delta R^2 \rangle}{\langle \delta V_J^2 \rangle} = \frac{4\alpha^2 I_B^2 R^2 k_B \Delta f / G}{4R k_B T \Delta f} = \frac{\alpha^2 I_B^2 R}{GT} = \alpha^2 \left(\frac{\Delta T_B}{T} \right) \quad (\text{B-22})$$

where ΔT_B is the heating associated with the bias current I_B . For this ratio to be greater than one, the dimensionless temperature coefficient should be large $\alpha \gg 1$.

Using this notation, we can compare several candidate materials for resistance bolometers. Simple metals at high temperatures show approximately power law temperature dependence:

$$R \propto T^a. \quad (\text{B-23})$$

For this case the temperature coefficient is simply:

$$\alpha = a. \quad (\text{B-24})$$

It is difficult to make sensitive bolometers from simple metals, because the exponent a is not large: typically $a \sim 1$.

The resistance of a common class of bolometer materials including carbon and vanadium oxide is characterized by variable range hopping for which:

$$R \propto \exp \left[(T_o/T)^{1/4} \right]. \quad (\text{B-25})$$

For this case the dimensionless temperature coefficient is:

$$\alpha = -\frac{1}{4} \left(\frac{T_o}{T} \right)^{1/4}. \quad (\text{B-26})$$

For variable range hopping it is difficult to achieve large temperature coefficients α even if T_o/T is large, due to the exponent $1/4$.

Semiconductors are another candidate material. For this case the resistance decreases with temperature as:

$$R \propto \exp(E_{act}/k_B T) \quad (\text{B-27})$$

where E_{act} is the activation energy for free carriers. The dimensionless temperature coefficient is:

$$\alpha = -\frac{E_{act}}{k_B T}. \quad (\text{B-28})$$

For extrinsic semiconductors at low temperatures in the freezeout regime the activation energy is the donor or acceptor binding energy $E_{act} = E_B$. For this case it is possible to achieve very large dimensionless temperature coefficients at very low temperatures, for example $\alpha \sim 100$ for acceptors in Ge at $T = 0.3$ K, and very sensitive bolometers have been demonstrated.

For intrinsic semiconductors operating at higher temperatures, the activation energy is half the energy gap, $E_{act} = E_{gap}/2$. A lower limit to the operating temperature and an upper limit to α in this case is given by the transition to extrinsic behavior when the intrinsic carrier concentration becomes comparable to the impurity concentration. For intrinsic Ge at $T = 300$ K, the dimensionless temperature coefficient $\alpha \sim 10$.

A large temperature coefficient can be obtained at a particular temperature by selecting a bolometer material which undergoes an electronic

phase transition. High temperature superconductors are being developed as bolometers, because the resistance rapidly drops near the superconducting transition temperature T_c . For YBCO, the transition temperatures T_c can be made comparable to standard cooler temperatures $T \sim 80$ K, and temperature coefficients higher than conventional bolometer materials are possible. Honeywell has reported high T_c bolometers with temperature coefficients $(1/R)dR/dT = 0.2 \text{ K}^{-1}$ near $T = 70$ K, for which $\alpha \sim 14$. The resistive transition in this material is broad in order to reduce the requirement for temperature regulation. Much sharper transitions are obtained in high quality samples of high T_c materials. It is not necessary to use superconductors for bolometers, because only the resistance change is important. Other resistive transitions can be exploited. For example, the electrons in NbSe₃ undergo a phase transition to a charge density wave state at moderate temperatures, accompanied by a sharp increase in resistance.

C APPENDIX: THERMOELECTRIC MATERIALS

Thermoelectric materials are those in which the flow of heat is coupled to the electric current. Because electrons carry entropy as well as electrical charge, all normal conductors are thermoelectric to some extent. Good thermoelectric materials with relatively strong coupling between the thermal and electric currents are useful for applications ranging from solid state coolers, to temperature sensors, to power generation.

For this report, the most relevant applications of thermoelectric materials are in solid state coolers and bolometric infrared detectors. Solid state coolers using thermoelectric elements are compact and have no moving parts. However, their efficiency is relatively low, and present materials reach temperatures only ~ 200 K. Thermoelectric materials with better low temperature performance are needed to push the operating temperature lower. Thermoelectric materials can also be used for bolometric infrared sensors. The best thermoelectric materials perform better than simple thermocouples for this application, and uncooled microbolometer arrays using this approach are under development at the Jet Propulsion Laboratory. High temperature thermoelectrics operating at temperatures ~ 800 K can be used to generate electric power.

New low temperature thermoelectric materials are needed to make coolers capable of reaching temperatures below 200 K. Because the characteristics of thermoelectric materials have been thoroughly explored since the 1950s, this task is difficult. However the development of new classes of man-made materials – heterostructures and nanostructured materials – creates hope that better low temperature thermoelectrics may be discovered or designed. In order to provide a guide to desirable physical properties for new thermoelectric materials, we review the origins of thermoelectricity below.

To understand the physical mechanism responsible for thermoelectricity and to compare different materials, it is helpful to develop a simple model. Practical thermoelectrics are typically semimetals or heavily doped semiconductors. We consider a material with one type of carrier (electrons or holes) with charge q , effective mass m , and cubic crystal symmetry so that the electrical and thermal conductivity are isotropic. Detailed treatments of thermoelectricity including specific material properties are given in reviews (Mahan 1997, *CRC Handbook of Thermoelectrics* 1995) and textbooks (see Ziman 1972).

The thermoelectric effect occurs in all normal conductors because electrons (or holes) carry both electrical charge and heat. The entropy s per charge carrier is quite generally given by the expression:

$$s = \frac{\langle \varepsilon \rangle - \mu}{T} \quad (\text{C-1})$$

where $\langle \varepsilon \rangle$ is the energy per particle, μ is the chemical potential, and T is the absolute temperature. Equation (C-1) applies equally well to low density (non-degenerate) carrier gases in semiconductors and high density (degenerate) gases in metals. This expression arises in the derivation of the Boltzmann factor and can be found from the Helmholtz free energy :

$$s = \left(\frac{\partial S_s}{\partial N} \right)_{V,T} = \frac{1}{T} \left[\left(\frac{\partial U}{\partial N} \right)_{V,T} - \left(\frac{\partial F}{\partial N} \right)_{V,T} \right] \equiv \frac{\langle \varepsilon \rangle - \mu}{T}. \quad (\text{C-2})$$

Here U and S_s are the total thermal energy and entropy of a gas of N particles in volume V .

Because thermoelectricity is a transport phenomenon we consider the nonequilibrium distribution $f(p)$ of an ideal gas of particles under the action of an applied electric field \vec{E} , a gradient in chemical potential $\vec{\nabla}\mu$, and a temperature gradient $\vec{\nabla}T$. In the relaxation time approximation of the Boltzmann transport equation (see Ziman 1972):

$$f - f^0 = \left(-\frac{\partial f^0}{\partial \varepsilon} \right) \tau_p \vec{v} \cdot \left[q\vec{E} - \vec{\nabla}\mu - \left(\frac{\varepsilon - \mu}{T} \right) \vec{\nabla}T \right]. \quad (\text{C-3})$$

Here ε and \vec{v} are the particle energy and velocity for momentum \vec{p} . The three terms inside the square brackets are the three forces which produce particle transport: the electric force $q\vec{E}$, the diffusive force due to density gradients $-\vec{\nabla}\mu$, and a thermal force produced by temperature gradients $-[(\varepsilon - \mu)/T]\vec{\nabla}T$. It is the thermal force which is responsible for thermoelectricity.

Equation (C-3) assumes that the nonequilibrium distribution $f(p)$ of particles in momentum space remains near the thermal distribution $f^0(p)$ under the action of the applied forces, so that the change can be expressed as $f - f^0 = (-\partial f^0 / \partial \varepsilon) \Delta \varepsilon$. The energy $\Delta \varepsilon$ imparted to carriers of momentum \vec{p} by the force is the product of the force, the carrier velocity, and the momentum relaxation time τ_p as in Equation (C-3). We have also assumed that the collisions which relax the distribution are elastic, or energy conserving. An example of an elastic process is impurity scattering; examples of inelastic processes are electron-electron and electron-phonon scattering. Equation (C-3) can be used as the starting point for treating carrier transport in both metals and semiconductors. However, good metals generally make poor thermoelectric materials, so we assume that the particle gas is non-degenerate, i.e. that is a low density gas obeying Maxwell Boltzmann statistics:

$$f^0 = N_p \exp\left(\frac{\mu - \varepsilon}{k_B T}\right) \text{ with } \frac{\partial f^0}{\partial \varepsilon} = -\frac{1}{k_B T} f^0 \quad (\text{C-4})$$

where N_p is the density of states in p-space.

One can understand the origin of the thermal force by noting that particles move more rapidly in hotter regions of the sample, and thus tend to escape a given region faster than they are replaced by cold particles, producing a particle current flowing from hot to cold. The coefficient which determines the strength of thermal force is simply the entropy per particle s . For a non-degenerate gas:

$$s = \frac{\varepsilon - \mu}{T}. \quad (\text{C-5})$$

It is helpful to note that s is quite generally related to the chemical potential via the thermodynamic identity:

$$s = \left(\frac{\partial S_s}{\partial N} \right)_{T,V} = - \left(\frac{\partial^2 F}{\partial N \partial T} \right)_V = - \left(\frac{\partial \mu}{\partial T} \right)_{N,V}. \quad (\text{C-6})$$

Here S_s is the total entropy for N particles in volume V , and F is the Helmholtz free energy.

The electric current density \vec{J} produced by the sum of these forces is determined by the integral over momentum space:

$$\vec{J} = \frac{2q}{k_B T} \int d^3 p f^0 \tau_p \vec{v} \vec{v} \cdot \left[q \vec{E} - \vec{\nabla} \mu - \left(\frac{\varepsilon - \mu}{T} \right) \vec{\nabla} T \right]. \quad (\text{C-7})$$

One can gain insight into the physical origins of thermoelectricity without actually carrying out the integration. For isotropic materials the total electric current has the following form:

$$\vec{J} = \sigma (\vec{E} - \frac{1}{q} \vec{\nabla} \mu) - \sigma S \vec{\nabla} T \quad (\text{C-8})$$

where σ is the electrical conductivity, and S is the Seebeck coefficient, a material parameter which characterizes the thermoelectric current. The electric and diffusive forces are grouped together, because it is generally their sum which is measured in experiments (consider for example the ‘voltage’ across a pn junction diode).

The electrical conductivity is given by

$$\sigma = \frac{2q^2}{k_B T} \int d^3 p f^0 \tau_p \vec{v} \vec{v} \cdot \hat{e} \quad (\text{C-9})$$

where \hat{e} is a unit vector in the direction of the electric field. This expression can treat complex situations with momentum dependent relaxation times τ_p and densities of states N_p . One generally side steps these complications by defining a single effective scattering time τ and an effective mass m , which are related to microscopic processes via the integral above. We then get the well known expression:

$$\sigma = \frac{n q^2 \tau}{m} \quad (\text{C-10})$$

where n is the carrier concentration, and we have used $\langle v_x^2 \rangle = k_B T / m$ for the average component of velocity along the electric field.

In the same spirit, we can obtain an expression for the Seebeck coefficient S . The integral for σS is identical to that for the electrical conductivity σ , except for the additional factor $(\varepsilon - \mu)/T$. Assuming that the integrand is well-behaved, we simply move the physically relevant quantities outside, replacing the energy by the effective average value ε , and find:

$$S = \frac{1}{q} \left(\frac{\varepsilon - \mu}{T} \right) = \frac{s}{q}. \quad (\text{C-11})$$

As shown, the Seebeck coefficient is equal to the entropy per free carrier s divided by the charge q ; S can have either sign, and it is positive for positively charged carriers. This is a simple and important result which will allow us to assess the relative merits of different thermoelectric materials. However, one should keep in mind that useful thermoelectric materials may rely on more complex microscopic processes which violate simple rules.

A simple physical consequence of the thermal force can be found by evaluating Equation (C-8) for the situation in which a temperature gradient is set by a flow of heat through the material, but no electric current can flow:

$$\vec{E} - \frac{1}{q} \vec{\nabla} \mu = S \vec{\nabla} T. \quad (\text{C-12})$$

We see that thermal gradients in the absence of an electric current produce electric fields (more precisely the electrochemical field $\vec{E} - (1/q) \vec{\nabla} \mu$); the constant of proportionality is the Seebeck coefficient S . Hot carriers flow away from higher temperature regions of the sample more rapidly than they are replaced by colder carriers. This flow is offset by the electrochemical field coming from the build up of charge (\vec{E}) and carriers ($-\vec{\nabla} \mu$) in colder parts of the sample. If the carriers cannot flow out of the sample, the total current density must cancel in equilibrium leading to Equation (C-12). For metals the resulting electric field \vec{E} is typically much greater than the diffusive current and one can neglect the diffusive force $-\vec{\nabla} \mu$ in Equation (C-12); for

semiconductors inclusion of the diffusive force may be necessary (e.g. for the thermoelectric effect in inhomogeneous devices like pn junctions).

Just as a temperature gradient produces an electric current, an electric field produces a thermal current. For linear response the thermal current density \vec{J}_Q can be written in the form:

$$\vec{J}_Q = \sigma ST \left(\vec{E} - \frac{1}{q} \vec{\nabla} \mu \right) - K_{QE} \vec{\nabla} T \quad (\text{C-13})$$

where K_{QE} is the thermal conductivity for $\vec{E} = 0$. Note that K_{QE} is not the usual thermal conductivity K_Q that one measures in the absence of electric currents; we return to this point later. The coefficient of the electrochemical field contains precisely the same factor σS that appears in Equation (C-8) for the electrical current density. This is no accident, but an exact symmetry which follows from time-reversal symmetry in the underlying equations of motion, an example of an Onsager relation (see Landau and Lifshitz 1969).

One can understand the physical origin of heat transport by carriers by noting that the heat carried per particle in a flow of charge carriers is:

$$\Delta Q = Ts = qST \quad (\text{C-14})$$

where s is the entropy per carrier, and we have used Equation (C-11) for the Seebeck coefficient S . Thus the heat current produced by an electric current with $\vec{\nabla} T = 0$ is given by:

$$\vec{J}_Q = ST \vec{J} = \sigma ST \left(\vec{E} - \frac{1}{q} \vec{\nabla} \mu \right) \quad (\text{C-15})$$

in agreement with Equation (C-13).

Equations (C-8) and (C-13) together are a starting point for the theory of thermoelectric devices (see Mahan 1997). For applications, the natural variables are \vec{J} and $\vec{\nabla} T$, rather than $\vec{E} - (1/q) \vec{\nabla} \mu$ and $\vec{\nabla} T$. Eliminating $\vec{E} - (1/q) \vec{\nabla} \mu$ from Equation (C-13) using Equation (C-8) we find:

$$\vec{J}_Q = ST \vec{J} - K_Q \vec{\nabla} T \quad (\text{C-16})$$

where K_Q is the thermal conductivity for zero current density $\vec{J} = 0$:

$$K_Q = K_{QE} \left[1 - \left(\frac{\sigma S^2}{K_{QE}} \right) T \right]. \quad (\text{C-17})$$

This is the usual thermal conductivity that one determines in purely thermal measurements. The thermal conductivity K_Q is smaller than K_{QE} , because the heat carried by the particle current is subtracted.

An important figure of merit for thermoelectric materials is the quantity Z which has dimensions of inverse temperature:

$$Z = \frac{\sigma S^2}{K_Q}. \quad (\text{C-18})$$

The efficiency of thermoelectric coolers is determined by the dimensionless product ZT which must be comparable or greater than one for good performance (see Mahan 1997). In the limit $ZT \gg 1$ the cooling efficiency approaches the ideal Carnot efficiency. The best current thermoelectric materials have $ZT \sim 1$.

We are now in a position to evaluate the promise of thermoelectric materials based on their physical characteristics. A good starting point is the Seebeck coefficient for nondegenerate carriers:

$$S = \frac{k_B}{q} \left(\frac{3}{2} - \frac{\mu}{k_B T} \right) \quad (\text{C-19})$$

where we have used $\varepsilon = (3/2)k_B T$, and the constant $k_B/q = 86\mu\text{V/K}$. The chemical potential is:

$$\mu = k_B T \ln \left(\frac{n}{n_Q} \right), \quad \text{with} \quad n_Q = g \left(\frac{m k_B T}{2\pi \hbar^2} \right)^{3/2}. \quad (\text{C-20})$$

Here n_Q is the quantum concentration (effective density of states), with g the product of the spin and valley degeneracies. For example $g = 12$ for n-type Si, which has spin 1/2 and six electron valleys. By definition, $n < n_Q$ for nondegenerate carriers, and $\mu < 0$. The chemical potential for semiconductors is determined by the dopant concentrations as well as the quantum concentration (see Seeger 1988, Sze 1981).

It is instructive to consider the temperature dependence of the Seebeck coefficient through the chemical potential for an n-type semiconductor with donor concentration N_D . At high temperatures the material is intrinsic with equal electron and hole concentrations, and the chemical potential lies near the middle of the energy gap ε_g . Intrinsic semiconductors are not typically good thermoelectrics, because the Seebeck coefficients of electrons and holes subtract and tend to cancel. As the temperature falls to values $k_B T < \varepsilon_g/2$ the chemical potential rises toward the conduction band, and holes become the minority carrier. In this extrinsic regime, most useful for thermoelectrics, the electron concentration is constant and equal to the donor concentration. At sufficiently low temperatures the chemical potential becomes pinned at the donor binding energy $-B$, and the carrier concentration freezes out exponentially. From this development we see that the Seebeck coefficient for nondegenerately doped semiconductors increases with temperature until the transition to intrinsic behavior is approached. Mahan (1997) gives an empirical rule that the best operating temperature for semiconductor thermoelectrics is $k_B T \sim \varepsilon_g/10$ in agreement with these arguments.

Good thermoelectric materials must have high electrical conductivity σ as well as a large Seebeck coefficient S , so that the figure of merit ZT can be as large as possible. High electrical conductivity increases the cooling power by increasing the flow of particles (and entropy) for a given applied voltage. The product appearing in the numerator of Z is called the power factor:

$$\sigma S^2 = \frac{n\tau}{m} \left(\frac{3}{2} - \ln \left(\frac{n}{n_Q} \right) \right)^2. \quad (\text{C-21})$$

Assuming τ is density independent, the power factor has a maximum at $\ln(n/n_Q) = -1/2$ for which the carrier density n is comparable to the quantum concentration n_Q . The condition $n \sim n_Q$ also marks the boundary above which the gas of carriers becomes degenerate and obeys Fermi-Dirac statistics. Materials having this property are heavily doped semiconductors and semimetals. The magnitude of the Seebeck coefficient at maximum power

factor $S = 2k_B/q = 170\mu\text{V/K}$ is typical of good thermoelectric materials (Mahan 1997).

The influence of the effective mass m on the performance of thermoelectric materials can be examined by evaluating the power factor at its maximum at $n = n_Q e^{-1/2}$:

$$(\sigma S^2)_{\max} = \frac{4}{e^{1/2}} \frac{k_B \tau}{m} n_Q \propto m^{1/2} T^{3/2}. \quad (\text{C-22})$$

As shown, the maximum power factor increases with the effective mass m and temperature T , because the quantum concentration is larger and greater carrier concentrations are possible. A heavy effective mass, or high density of states at the Fermi surface, is generally desirable for thermoelectric materials. Unfortunately, small bandgap semiconductor materials which could be useful thermoelectrics at room temperature and below tend to have light effective masses.

Thermal conductivity is the final major factor influencing the performance of thermoelectric materials. Low thermal conductivity improves the efficiency of thermoelectric coolers by reducing unwanted reverse heat flow. The total thermal conductivity K_Q is the sum of contributions from charge carriers and from phonons. Because phonons do not contribute to the thermoelectric effect or the cooling power, the best performance would be obtained if it were possible to eliminate heat conduction by phonons, and free carriers were responsible for the transport of both charge and heat. For good metals with $n \sim 10^{23} \text{ cm}^{-3}$ this is the case, but for heavily doped semiconductors and semimetals with much lower carrier concentrations $n \sim 10^{19} \text{ cm}^{-3}$, phonons typically dominate thermal conduction. Nonetheless it is interesting to examine the effects of heat conduction by free carriers. The thermal conductivity of a nondegenerate carrier gas is (see Kittel 1971):

$$K_Q = \frac{1}{3} C v^2 \tau = \frac{3}{2} \frac{n \tau}{m} k_B^2 T \quad (\text{C-23})$$

where C is the heat capacity per unit volume. Because carriers transport both charge and heat, the ratio of thermal to electrical conductivity is a

constant:

$$\frac{K_Q}{\sigma} = \frac{(3/2)k_B^2 T}{q^2} = \frac{3}{2} \left(\frac{k_B}{q} \right)^2 T. \quad (\text{C-24})$$

This relation is known as the Wiedemann-Franz law. [For good metals it takes a slightly different form due to the difference in carrier statistics: $K_Q/\sigma = (\pi^2/3)(k_B/q)^2 T$.] Inserting Equation (C-24) into Equation (C-18) we get an upper limit to the figure of merit:

$$ZT = \frac{2}{3}(qS)^2 = \frac{2}{3} \left(\frac{s}{k_B} \right)^2. \quad (\text{C-25})$$

Using typical values for the entropy per particle $s/k_B \sim 1$ in this expression, one finds that values $ZT > 1$ are difficult to obtain, in agreement with practical experience.

Given that phonons dominate the thermal conductivity K_Q of most thermoelectric materials, one would like to reduce K_Q by decreasing the population of phonons and by increasing their scattering rate. At high temperatures all thermal modes are excited, but below the Debye temperature T_D higher energy modes begin to freeze out. For a cubic monatomic crystal with atomic concentration n_A we have:

$$T_D = \frac{\hbar c_s}{k_B} (6\pi^2 n_A)^{1/3}. \quad (\text{C-26})$$

Because atomic concentrations for most materials are comparable, differences in Debye temperature arise from differences in the speed of sound c_s . Typical values of the Debye temperature for thermoelectric materials range from below room temperature ($T_D = 120$ K for Bi) to above ($T_D = 645$ K for Si). A hypothetical low temperature thermoelectric material for coolers might be able to gain in performance by operating well below T_D . Unfortunately, the small bandgap materials which are the best candidates tend to be soft materials with low Debye temperatures, like Bismuth.

Thermoelectric performance can also be improved by introducing mechanisms for phonon scattering where possible. Skudderudite materials, which

are good high temperature thermoelectrics, have a large and complex unit cell with relatively large open spaces. Phonon scattering can be increased by 'filling' these spaces with otherwise inert atoms. The added atoms move relatively freely and act as scatterers for phonons in the basic lattice (see Mahan 1997).

D APPENDIX: WORKSHOP PARTICIPANTS

| | |
|------------------------|-------------------------------|
| Jack Ahearn | Lockheed Martin -Sanders |
| Ray Balcerak | DARPA |
| Michael Blessinger | Raytheon Amber |
| Kwong-Kit Choi | Army Research Laboratory |
| C. Art Cockrum | Santa Barbara Research Center |
| Roger DeWames | Rockwell Science Center |
| Mildred S. Dresselhaus | MIT |
| Charles Hansom | Texas Instruments |
| Timothy Krabach | Jet Propulsion Laboratory |
| Paul Kruse | Infrared Solutions |
| Yu-Haw Lo | Cornell University |
| Chip Marshall | Lockheed Martin |
| Aaron Penkacik | Lockheed Martin |
| William Radford | Santa Barbara Research Center |
| James Robinson | Texas Instruments |

References

- [1] *CRC Handbook of Thermoelectrics*, D.M. Rowe, ed. (CRC Press, Boca Raton, 1995).
- [2] C. A. Cockrum, "HgCdTe material properties and their influence on IR FPA performance", *Proc. SPIE*, **2685**, 2 (1996).
- [3] C. Kittel, *Introduction to Solid State Physics*, 4th Ed. (John Wiley, New York, 1971).
- [4] P. W. Kruse, "A Comparison of the limits to the performance of thermal and photon detector imaging arrays", *Infrared Phys. Technol.* **36**, 869 (1995).
- [5] P. Kruse and D. Skatrud, Eds., *Semiconductors and Semimetals vol. XX*, (Academic Press, New York, 1997).
- [6] G. D. Mahan, "Good Thermoelectrics", *Solid State Physics vol. XX*, H. Ehrenreich ed. (Academic Press, New York, 1997).
- [7] K. Seeger, *Semiconductor Physics*, 4th Ed. (Springer-Verlag, Berlin, 1988).
- [8] S. M. Sze, *Physics of Semiconductor Devices* (John Wiley, New York, 1981).
- [9] R. Westervelt, J. Sullivan, and N. Lewis, "Imaging Infrared Detectors", JASON report JSR-91-600 (1992).
- [10] J. M. Ziman, *Principles of the Theory of Solids*, 2nd Ed. (Cambridge Univ. Press, New York, 1972).

DISTRIBUTION LIST

Director of Space and SDI Programs
SAF/AQSC
1060 Air Force Pentagon
Washington, DC 20330-1060

CMDR & Program Executive Officer
U S Army/CSSD-ZA
Strategic Defense Command
PO Box 15280
Arlington, VA 22215-0150

Superintendent
Code 1424
Attn Documents Librarian
Naval Postgraduate School
Monterey, CA 93943

DTIC [2]
8725 John Jay Kingman Road
Suite 0944
Fort Belvoir, VA 22060-6218

Dr. A. Michael Andrews
Director of Technology
SARD-TT
Room 3E480
Research Development Acquisition
103 Army Pentagon
Washington, DC 20301-0103

Dr. Albert Brandenstein
Chief Scientist
Office of Nat'l Drug Control Policy
Executive Office of the President
Washington, DC 20500

Dr. H. Lee Buchanan, III
Assistant Secretary of the Navy
(Research, Development & Acquisition)
3701 North Fairfax Drive
1000 Navy Pentagon
Washington, DC 20350-1000

Dr. Collier
Chief Scientist
U S Army Strategic Defense Command
PO Box 15280
Arlington, VA 22215-0280

D A R P A Library
3701 North Fairfax Drive
Arlington, VA 22209-2308

Dr. Martin C. Faga
President and Chief Exec Officer
The MITRE Corporation
A210
202 Burlington Road
Bedford, MA 01730-1420

Mr. Frank Fernandez
Director
DARPA/DIRO
3701 North Fairfax Drive
Arlington, VA 22203-1714

Mr. Dan Flynn [5]
Program Manager
DI/OT/SAB
DI/OTI/SAG
5 S 49 NHB
Washington, DC 20505

Dr. Paris Genalis
Deputy Director
OUSD(A&T)/S&TS/NW
The Pentagon, Room 3D1048
Washington, DC 20301

Dr. Lawrence K. Gershwin
NIO/S&T
2E42, OHB
Washington, DC 20505

DISTRIBUTION LIST

General Thomas F. Gioconda [5]
Assistant Secretary for Defense
US Department of Energy
DP-1, Room 4A019
Mailstop 4A-028
1000 Independence Ave, SW
Washington, DC 20585

Mr. Lee Hammarstrom
National Reconnaissance Office
14675 Lee Road
Chantilly, VA 20151

Dr. Theodore Hardebeck
STRATCOM/J5B
Offutt AFB, NE68113

Mr. David Havlik
Manager
Weapons Program Coordination Office
MS 9006
Sandia National Laboratories
PO Box 969
Livermore, CA94551-0969

Dr. Helmut Hellwig
Deputy Asst Secretary
(Science, Technology and Engineering)
SAF/AQR
1060 Air Force Pentagon
Washington, DC 20330-1060

Dr. Robert G. Henderson
Director
JASON Program Office
The MITRE Corporation
1820 Dolley Madison Blvd
McLean, VA 22102

J A S O N Library [5]
The MITRE Corporation
Mail Stop W002
1820 Dolley Madison Blvd
McLean, VA 22102

Mr. O' Dean P. Judd
Los Alamos National Laboratory
Mailstop F650
Los Alamos, NM 87545

Dr. Bobby R. Junker
Office of Naval Research
Code 111
800 North Quincy Street
Arlington, VA 22217

Dr. Martha Krebs
Director
Energy Research, ER-1, Rm 7B-058
1000 Independence Ave, SW
Washington, DC 20858

Lt Gen, Howard W. Leaf, (Retired)
Director, Test and Evaluation
HQ USAF/TE
1650 Air Force Pentagon
Washington, DC 20330-1650

Dr. George Mayer
Scientific Director
Army Research Office
4015 Wilson Blvd
Tower 3, Suite 216
Arlington, VA 22203-2529

Ms. M. Jill Mc Master [3]
Central Intelligence Agency
DS&T/IPO
2S30, Plaza A
Washington, DC 20505

Dr. Thomas Meyer
DARPA/DIRO
3701 N. Fairfax Drive
Arlington, VA 22203

Dr. Julian C. Nall
Institute for Defense Analyses
1801 North Beauregard Street
Alexandria, VA 22311

DISTRIBUTION LIST

Major General John S. Parker
U.S. Army Medical Research and Material
Command
504 Scott Street
Ft Detrick, MD 21702-5012

Dr. Ari Patrinos [5]
Associate Director
Biological and Environmental Research
SC-70
US Department of Energy
19901 Germantown Road
Germantown, MD 207874-1290

Dr. Bruce Pierce
Ballistic Missile Defense Org
BMDO/TO
7100 Defense Pentagon
Room 1E108
Washington, DC 20301-7100

Mr. John Rausch [2]
Division Head 06 Department
NAVOPINTCEN
4301 Suitland Road
Washington, DC 20390

Records Resource
The MITRE Corporation
Mail Stop W115
1820 Dolley Madison Blvd
McLean, VA 22102

Dr. Fred E. Saalfeld
Director
Office of Naval Research
800 North Quincy Street
Arlington, VA 22217-5000

Dr. Dan Schuresko
Chief
Advanced Technology Group/
Community Management
Washington, DC 20505

Dr. John Schuster
Submarine Warfare Division
Submarine, Security & Tech
Head (N875)
2000 Navy Pentagon Room 4D534
Washington, DC 20350-2000

Dr. Richard Spinrad
US Naval Observatory
Naval Oceanographers Office
3450 Massachusetts Ave, NW
Washington, DC 20392-5421

Dr. Michael A. Strosio
US Army Research Office
P. O. Box 12211
Research Triangle Park, NC 27709-2211

Dr. George W. Ullrich [3]
ODUSD(S&T)
Director for Weapons Systems
3080 Defense Pentagon
Washington, DC 20301-3080

Dr. David Whelan
Director
DARPA/TTO
3701 North Fairfax Drive
Arlington, VA 22203-1714

Dr. Peter D. Zimmerman
Science Advisor
ACDA
320 21st Street, NW
Washington, DC 20451